Novel dihydropteridinone derivatives as potent and selective inhibitors of the understudied human vaccinia-related kinase 1 (VRK1)

Fernando H. de Souza Gama, [1#] Luiz A. Dutra, [2#] Michael Hawgood, [3,4] Caio Vinícius dos Reis, [2,5] Ricardo A. M. Serafim, [2,6] Marcos A. Ferreira Jr, [1 2] Bruno V. M. Teodoro, [1] Jéssica Emi Takarada, [2] André S. Santiago, [2] Vitor M. Almeida, [2,7] Carina Gileadi, [2] Priscila Z. Ramos, [2] Anita Salmazo, [2,8] Stanley N. S. Vasconcelos, [2] Micael R. Cunha, [2] Dimitrios-Ilias Balourdas, [9] Susanne Mueller, [9] Stefan Knapp, [9] Katlin B. Massirer, [2] Jonathan M. Elkins, [2,10] Opher Gileadi, [2,11] Alessandra Mascarello, [1] Bennie B. L. G. Lemmens, [3,4] Cristiano R. W. Guimarães, [*1,12] Hatylas Azevedo, [1] Rafael M. Couñago [*2,13]

[1] Aché Laboratórios Farmacêuticos S.A., Guarulhos, São Paulo, 07034-904, Brazil.

[2] Centro de Química Medicinal, Centro de Biologia Molecular e Engenharia Genética, Universidade Estadual de Campinas, Av. Dr. André Tosello 550, 13083-886 Campinas, São Paulo, Brazil.

[3] Science for Life Laboratory, Sweden, Tomtebodavägen 23A, 17165 Solna, Sweden

[4] Division of Genome Biology, Department of Medical Biochemistry and Biophysics, Karolinska Institutet, SE-17177 Stockholm, Sweden.

[5] Department of Biochemistry, University of Cambridge, Sanger Building, 80, Tennis Court Road, CB2 1QW, Cambridge, UK

[6] Present address: Department of Pharmaceutical/Medicinal Chemistry, Eberhard Karls University Tübingen, Auf der Morgenstelle 8, 72076 Tübingen, Germany.

[7] Present address: Eurofarma Laboratórios S/A, 06696-000-Itapevi, SP, Brazil.

[8] Present address: Institute of Science and Technology Austria, 3400 Klosterneuburg, Austria.

[9] Institute of Pharmaceutical Chemistry, Johann Wolfgang Goethe University, Max-von-Laue-Str. 9, Frankfurt am Main, 60438, Germany; Structural Genomics Consortium (SGC), Buchmann Institute for Life Sciences, Johann Wolfgang Goethe University, Max-von-Laue-Str. 15, Frankfurt am Main, 60438, Germany.

[10] Present address: Centre for Medicines Discovery, Nuffield Department of Medicine, University of Oxford, NDM Research Building, Roosevelt Drive, Oxford, OX3 7FZ, UK

[11] Present address: Structural Genomics Consortium and Centre for Molecular Medicine, Karolinska Institutet, S-171 76 Stockholm, Sweden.

[12] Nintx (Next Innovative Therapeutics), Av. das Nações Unidas 18801, São Paulo 04757-025, Brazil.

[13] Present address: Structural Genomics Consortium and Division of Chemical Biology and Medicinal Chemistry, UNC Eshelman School of Pharmacy, University of North Carolina, Chapel Hill, North Carolina 27599, USA.

# These authors contributed equally to this paper.

* Corresponding author: rafael.counago@unc.edu

ABSTRACT

The human Vaccinia-Related Kinase 1 (VRK1) is highly expressed in various tumor types and plays important roles in cell proliferation and the maintenance of genome integrity. While prior genetic studies indicate that VRK1 inhibition offers therapeutic potential, especially in cancers deficient in VRK2 expression or DNA damage repair, the current lack of suitable VRK1 inhibitors hampers the validation of this kinase as a therapeutic target and the translation of these findings to the clinic. Here, we developed novel VRK1 inhibitors based on BI-D1870, a pteridinone inhibitor of RSK kinases. Our optimized VRK1 inhibitor displays improved kinome-wide selectivity, and effectively mimic cellular outcomes of VRK1 depletion. Notably, VRK1 inhibition triggered severe mitotic errors and genome instability in p53-deficient cells. Together, our findings highlight the potential of VRK1 inhibition in treating p53-deficient tumors and possibly enhancing the efficacy of existing cancer therapies that target DNA stability or cell division.

INTRODUCTION

The human Vaccinia-Related Kinase (VRK) family consists of serine/threonine protein kinases first identified by their similarity to the vaccinia virus B1 kinase. [1,2] Human VRK1 and VRK2 are the two active members of the VRK family, whereas VRK3 is a pseudokinase. [3] Several studies have highlighted the therapeutic potential of inhibiting VRK1. VRK1 is overexpressed in various solid tumors and has been linked to a poor prognosis in patients with breast cancer and glioma. [4–13] Conversely, reducing VRK1 levels via genetic tools, such as shRNA, leads to cell death in a variety of tumors and enhances the efficacy of chemotherapeutic agents like temozolomide and olaparib, which induce DNA damage. [8,14–16] The effects of reducing VRK1 levels are more pronounced in tumor cells deficient in VRK2 expression, likely due to VRK2's ability to compensate for the lack of VRK1. [17,18]

VRK1's role in modulating key proteins, such as BAF (Barrier-to-autointegration factor), during cell division is crucial for tumor cell survival. [19] BAF is a small protein, made up of 89 amino acids, that is found in both the nucleoplasm and the nuclear envelope. It plays a critical role in safeguarding genome integrity and ensuring successful completion of mitosis. [20,21] Central to these functions is BAF's ability to bind DNA and its numerous protein partners, which can be altered through phosphorylation. BAF phosphorylation allows it to detach from chromatin and nuclear envelope proteins, which in turn aids the dissolution of the nuclear envelope during mitosis. [19,22–27] Thus, VRK1 knockdown deregulates BAF function, resulting in abnormal nuclear envelope formation, DNA damage, cell cycle arrest, and apoptosis. [17,18]

Furthermore, the role of VRK1 in the DNA damage response is essential for tumor cell survival. VRK1 is implicated in the DNA damage response through the phosphorylation of p53 and H2AX. [23,25,28–31] p53 is a tumor suppressor protein that plays a critical role in responding to both external and internal stresses, including DNA damage. [32,33] The gene coding for the p53 protein is the most frequently mutated gene in human cancers. [34,35] Loss of p53 function permits the accumulation of DNA damage in cancer cells, increasing their survival by failing to trigger apoptosis or cellular senescence. [36] Similarly, phosphorylated histone H2AX plays a vital role in the early DNA damage response by recruiting components such as NBS1 (Nijmegen Breakage Syndrome 1) and the kinase ATM (Ataxia Telangiectasia Mutated) to DNA break sites. [25] Thus, VRK1 deficiency fuels genome instability in two ways; firstly by compromising mitotic fidelity and chromosome stability and secondly by abrogating DNA damage checkpoint signaling.

Despite these promising observations, there are currently no high-quality chemical tools available to pharmacologically validate VRK1 as a drug target in cancer. Our group has previously identified a pyridine derivative (compound **26** in REF[37]) and the racemic pteridinone BI-D1870 (Figure 1) as potent VRK1

inhibitors and determined co-crystal structures of VRK1 bound to both compounds. [37,38] Originally, BI-D1870 was developed to inhibit the N-terminal kinase domain of p90 ribosomal S6 kinases exhibiting IC_{50} values against those kinases between 10-30 nM. [39,40] Additionally, BI-D1870 was found to bind to BRD4, a member of the Bromodomain family of human proteins, albeit with a low affinity of approximately 3.5 µM. [41] Notably, BI-D1870 exhibited 30-100-fold reduced potency in cells compared to its action against isolated RSK kinases *in vitro*. The reduced efficacy of ATP-competitive kinase inhibitors in cells often results from the high intracellular ATP concentrations, which can range from 1–10 mM. [42,43]

In the current study, we describe the rational optimization of BI-D1870 derivatives as potent, selective, and cell-active VRK1 inhibitors. These novel VRK1 inhibitors have improved potency, selectivity, and pharmacokinetic properties compared to BI-D1870. To facilitate the interpretation of cell-based assays using these compounds, we also generated a structurally similar VRK1-inactive compound as a negative control. Using these novel chemical tools, we demonstrated that pharmacological inhibition of VRK1 disrupted cell cycle progression and genome integrity. We expect these novel chemical tools to deepen our understanding of VRK1's cellular role and accelerate the validation of this human kinase as a potential therapeutic target.

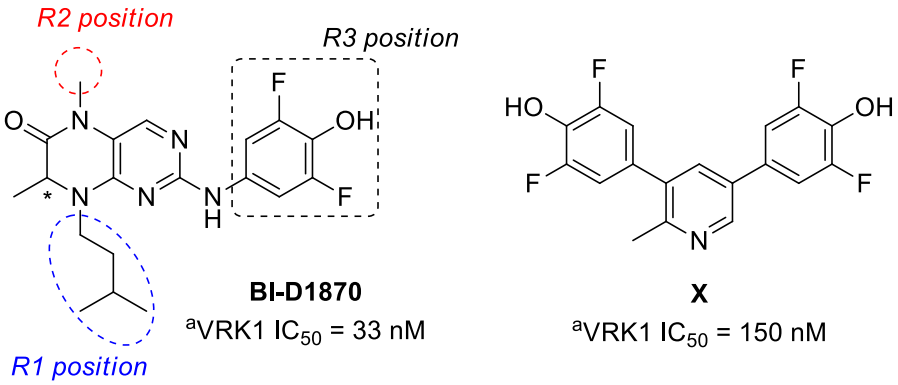

Figure 1 - Chemical structures of VRK1 inhibitors. The stereogenic center (star) and positions R1, R2 and R3 in BI-D1870 are indicated. BI-D1870 and compound **26** from REF[37].

RESULTS AND DISCUSSION

DESIGN

Analysis of co-crystal structures of human proteins bound to ligands with the BI-D1870 2-amino-dihydropteridinone core suggested potential development of this compound as a selective VRK1 inhibitor. [44] The co-structure of BI-D1870 bound to VRK1 revealed two distinct ligand poses within the kinase ATP-binding pocket, termed *canonical* and *alternative* (Supplementary Figures S1A, B). In the canonical binding pose, the amide methyl group in BI-D1870 2-amino-dihydropteridinone core (substituent **R2**) pointed towards a solvent-accessible opening between the hinge region (residues 132-136) and the base of the P-Loop (residues 44-49) close to the entrance of VRK1 ATP-binding site (Supplementary Figure S1A). The co-crystal structure of BI-D1870 bound to RSK2, which is the ligand's presumed target in cells, [45] also showed the inhibitor in the canonical binding pose (Supplementary Figure S1C). However, most co-crystal structures of other protein kinases with compounds containing the BI-D1870 2-amino-dihydropteridinone core displayed ligands in the alternative pose (Supplementary Figure S1D and Supplementary Table S1). In the alternative binding pose, substituents in **R2** point directly towards the kinase hinge region (Supplementary Figure S1B). Based on these findings, we hypothesized that larger substituents in **R2** could promote BI-D1870 analogues to preferentially adopt the canonical pose within the VRK1 ATP-binding site, resulting in more selective compounds. Further, these structural analyses also suggested there was available space within the VRK1 ATP-binding pocket to explore the *R*-form of BI-D1870 stereogenic center (Supplementary Figure S2A).

CHEMISTRY

To test these hypotheses, we used the D- or L-alanine amino acid to synthesize a set of (*R*)- or (*S*)-pteridinone derivatives using the synthetic route shown in Scheme 1. The intermediate (D)- or (L)-alanine methyl ester hydrochloride (ii) was obtained by esterification of (D)- or (L)-alanine (i) using thionyl chloride in methanol at low temperature, followed by an aromatic nucleophilic substitution using 2,4-dichloro-5-nitropyrimidine by using potassium carbonate and diethylether:water (1:1) as solvent. The intermediate (iii) was obtained through nitro-reduction using iron powder in acetic acid as solvent, followed by cyclization through the reaction between the aromatic amine (obtained in situ) and methyl ester moiety. Afterwards, the intermediate iv was obtained through bis N-alkylation using NaH 60% oil mineral using dimethylformamide as solvent at low temperature. Finally, we achieved the synthesis of (*R*)/(*S*)-pteridinone derivatives **1**-**42** (compound **42** is a negative control and referred to as **VRK-N**, see below) by reacting intermediate (iv) with the respective aniline derivatives in a strongly acidic condition.

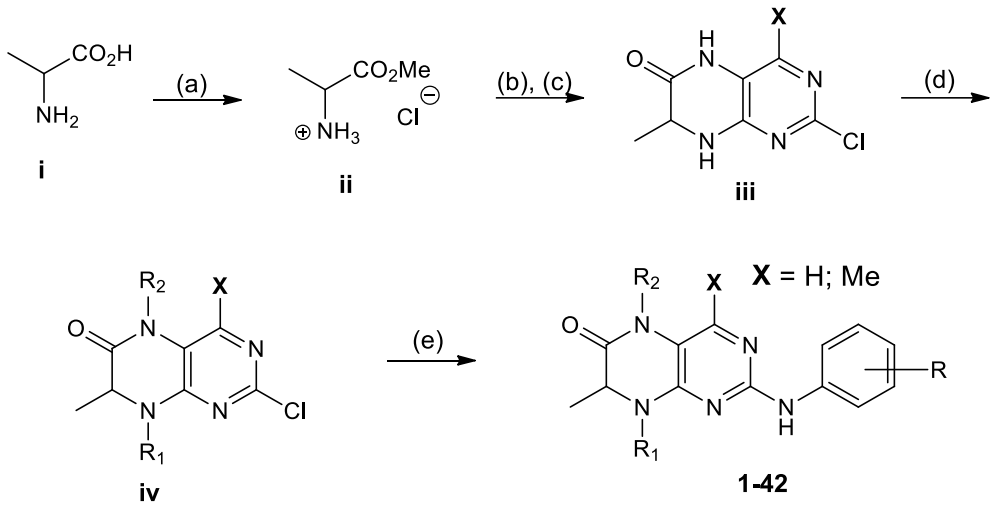

Scheme 1. Synthesis of dihydropteridinone derivatives. (a) $SOCl_2$, methanol, 0°C → room temperature, overnight. (b) K_2CO_3, diethylether:water (1:1), room temperature, overnight. (c) iron powder, acetic acid, room temperature, overnight. (d) alkyl bromide, NaH, DMF, 1h, 0°C → room temperature. (e) anilines, 80% ethanol, HCl, reflux, 12h.

PROTEIN BIOCHEMISTRY AND BI-D1870 ACTIVITY ON VRK1 AND VRK2

To assess the inhibitory potency of the novel dihydropteridinone derivatives against VRK1 and its close homologue VRK2, we developed TR-FRET-based enzymatic assays. These assays utilized a generic peptide derived from the human histone H3 sequence, a known VRK1 substrate [29] and commercially available, full-length VRK1 and VRK2 (Supplementary Figure S3A-D). These assays enabled us to determine $K_{M,ATP}$ values for VRK1 (3.1 µM) and VRK2 (9.8 µM). Utilizing the Cheng-Prusoff equation, we calculated the inhibitory constants (K_i) from the IC_{50} values, which were obtained through non-linear regression analysis of experimental data (Supplementary Table S2). Our results confirmed that BI-D1870 is a potent inhibitor of both VRK1 and VRK2, with K_i values of 56.1 and 28.0 nM, respectively (Supplementary Table S2; Supplementary Figure S3E).

DEVELOPMENT OF POTENT VRK1 INHIBITORS

To determine the impact of different **R1** and **R2** substituents on VRK1 kinase activity, we synthesized a series of (*R*)-2-amino-dihydropteridinone analogues (Table 1). Compared to the racemic BI-D1870, the (*R*)-enantiomer (compound **1**) showed approximately 2-fold lower potency towards VRK1 (K_i = 100.7 nM; Figure 2A). Nevertheless, replacing the methyl group at the **R2** position of **1** with a propargyl (**2**) led to a ~3-fold potency gain (K_i = 31.5 nM) (Figure 2A). The co-crystal structure of VRK1 bound to **2** (PDB ID 6CNX; Figure 2B-D, Supplementary Table S3) confirmed that the compound adopted the canonical binding pose, with its **R2** propargyl group directed into the space between the hinge region and the kinase P-Loop. The rigid propargyl group of **2** was accommodated by a positively charged pocket formed by Arg133 in the kinase hinge region and residues within VRK1 P-Loop (Figure 2B). It is worth noting that the P-Loop represents a flexible and structurally conserved segment within the kinase domain, often appearing disordered in various protein kinase crystal structures. Nevertheless, in complex with **2**, the VRK1 P-loop folded over the ligand, with the side chain of P-Loop residue Phe48 facing the methyl group attached to the compound stereogenic center, which was accommodated by a cavity within the bottom of VRK1 ATP-binding site. Additionally, π-stacking interactions involving the carbonyl residue of arginine and the *sp*-hybridized orbitals of the propargyl group might play a role in the enhanced potency of compound **2** over **1.**

Table 1 - Structure and activity of (*R*)-2-amino-dihydropteridinone derivatives having changes in R1 and R2

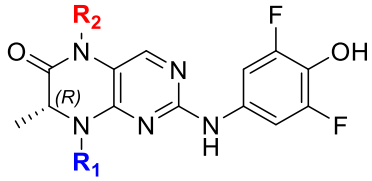

Entry	R1	R2	K_i (nM) [a]
1	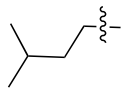	Me	100.7 (77.1 - 131.5)
2	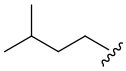	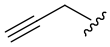	31.5 (24 - 41.4)
3	Me	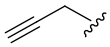	194.1 (119.1 - 316.2)
4		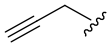	36.7 (1.6 - 855.1)
5		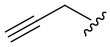	31.0 (27.8 - 34.6)
6	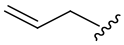	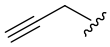	31.7 (22.5 - 44.7)
7	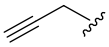	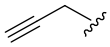	33.8 (29.7 - 38.4)
8		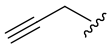	23.1 (20.6 - 26)
9		Me	66.5 (39.3 - 112.7)
10	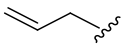	Me	213.8 (98.4 - 463.4)
11	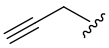	Me	134.6 (95.1 - 190.1)
12	Bn	Me	128.8 (37.2 - 446.7)
13	Me	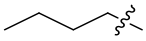	128.2 (108.4 - 151.7)
14	Me	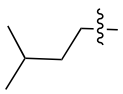	183.2 (21.5 - 1563.1)
15	Me	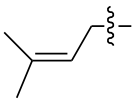	121.1 (90.8 - 161.1)
16	Me	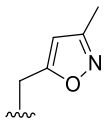	126.8 (75.9 - 211.3)
17	Me	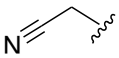	66.2 (50.6 - 86.7)

[a] inhibition constants calculated using the Cheng-Prusoff equation from IC_{50} values estimated from two independent experiments performed in duplicates; numbers in parenthesis are CI 90%; Bn – benzyl.

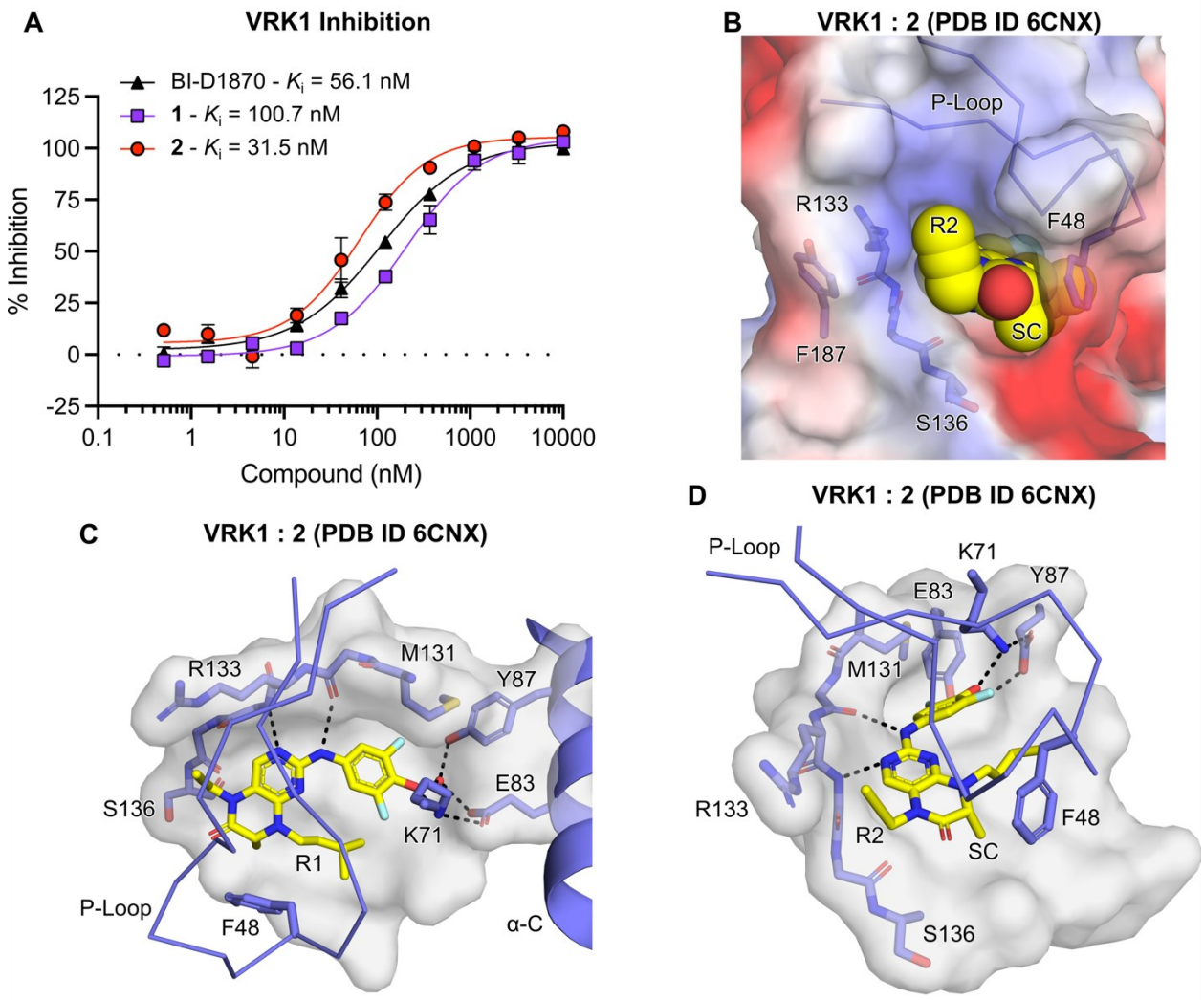

Figure 2. Inhibition of VRK1 by BI-D1870 derivatives and binding mode of propargyl derivative **2**. (A) Dose-response curves for racemic BI-D1870 and its (*R*)-pteridinone derivatives **1** and **2**. Data shown are mean ± SD of at least two independent experiments performed in duplicates. Indicated K_i values were obtained by applying the Cheng-Prusoff equation to IC_{50} values determined following fitting of the experimental data to the four-parameter sigmoidal dose-response equation. See Supplementary Table S2 for IC_{50} and SD values. (B-D) Co-crystal structure of **2** bound to VRK1. Substituents **R1**, **R2** and the stereogenic centre (SC) in **2** are indicated. Relevant residues and secondary structures around the enzyme ATP-binding site are indicated - α-helix C (blue cartoon), P-Loop (residues 39-55; blue ribbon), the hinge region (residues 132-136; sticks), the gate-keeper residue (M131), the catalytically important glutamate (E83) and lysine (K71) residues, F48 in the P-loop and Y87 in α-helix C. In B, molecular surfaces are colored by potential (kT/e - calculated by APBS [46] as implemented in PyMOL v. 2.6; red - negative; to blue - positive). In C, D, the bottom of VRK1 ATP-binding site is shown as a white (molecular) surface.

We exploited the increased potency of **2** to assess the impact of various **R1** substituents in (*R*)-2-amino-dihydropteridinone analogues containing a propargyl group in **R2** (compounds **3**-**8**; Table 1). Replacing the **R1** isopentyl moiety in **2** with a methyl group (**3**) led to a 3-fold potency decrease (K_i = 194.1 nM). Nevertheless, compounds having similar potencies to **2** were obtained by the addition of longer, aliphatic chains (saturated - **4** and **5**; or unsaturated - **6** and **7**/) or a cyclopropyl moiety in **R1** (**8**). Co-crystal structures of **3** (PDB ID 6CFM), **4** (PDB ID 6CQH), **7** (PDB ID 6CMM) and **8** (PDB ID 6VXU) bound to VRK1 confirmed these compounds adopted the canonical binding pose (Figure 3; Supplementary Table S3). As expected, in these co-crystal structures, the **R1** moieties of the ligands extended towards the protein P-Loop, which was found to be disordered in the co-crystals of VRK1 bound to compounds with linear chains (**3**, **4** and **7**). Conversely, the presence of the cyclopropyl moiety in **8** appeared to stabilize the protein P-loop, with the aromatic ring of residue Phe48 facing the compound's stereogenic center, as previously observed in the co-crystal of VRK1 bound to **2**. These findings demonstrated that (*R*)-2-amino-dihydropteridinone analogues were well tolerated by VRK1 and suggested the protein could accommodate **R1** substituents of varying lengths, bulk, and degrees of saturation.

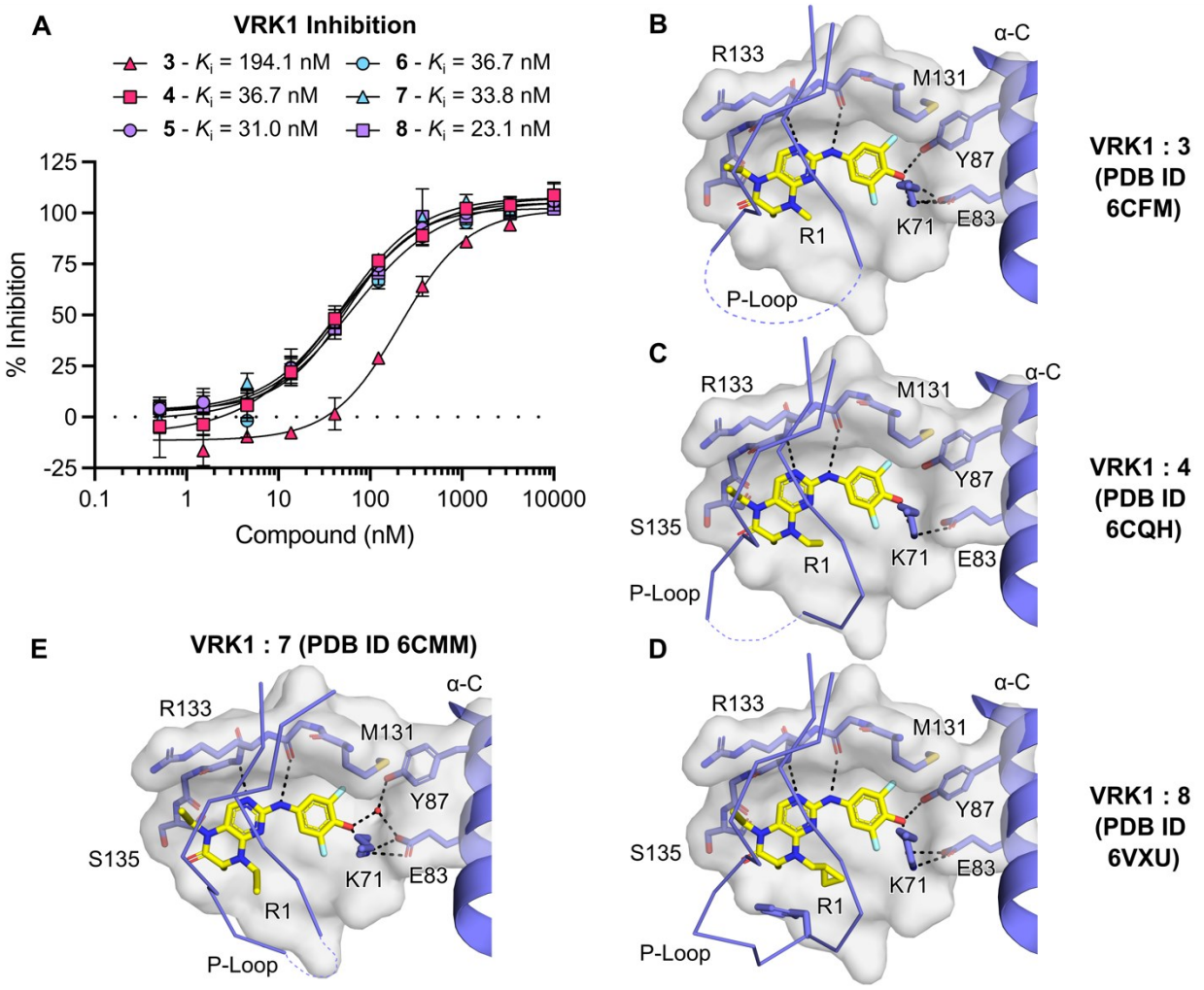

Figure 3. VRK1 inhibition by (*R*)-2-amino-dihydropteridinones **3**-**8** and binding mode of analogues **3**,**4**,**7** and **8**. (A) Dose-response curves for analogues **3**-**8**. Data shown are mean ± SD of at least two independent experiments performed in duplicates. Indicated K_i values were obtained by applying the Cheng-Prusoff equation to IC_{50} values determined following fitting of the experimental data to the four-parameter sigmoidal dose-response equation. See Supplementary Table S2 for IC_{50} and SD values. (B-E) Co-crystal structure of **3**, **4**, **7** and **8** bound to VRK1. Relevant residues and secondary structures around the enzyme ATP-binding site are indicated - α-helix C (blue cartoon), P-Loop (residues 39-55; blue ribbon), the hinge region (residues 132-136; sticks), the gate-keeper residue (M131), the catalytically important glutamate (E83) and lysine (K71) residues, F48 in the P-loop and Y87 in α-helix C. The bottom of VRK1 ATP-binding site is shown as a translucid, white (molecular) surface.

To better assess the contributions of a propargyl moiety in **R2** for compound potency, we replaced this group with a methyl to create matched pairs for analogues **5**, **6** and **7**, yielding compounds **9**, **10** and **11**. Our results showed these new compounds were 2 to 5-fold less potent than their counterparts having a propargyl in **R2** (K_i values for **9**-**11** ranged from 66.5 to 213.8 nM; Table 1; Supplementary Figure S4). The co-crystal structure of **11** bound to VRK1 (PDB ID 6VZH) confirmed that the inhibitor adopted the expected canonical binding mode, with the compound propargyl moiety in **R1** pointing towards the kinase P-Loop region, as previously seen for **7** (Figure 4A; Supplementary Table S3). These results indicated that a methyl group in place of the propargyl in **R2** led to decreased potency. Furthermore, we synthesized **12**, which has a benzyl group in **R1** and a methyl in **R2**, to investigate potential π-π interactions with the P-Loop residue Phe48 for enhanced potency. However, **12** (K_i = 128.8 nM) was found to be equipotent to the parent compound, (*R*)BI-D1870 (**1**), suggesting that adding a benzyl ring to **R1** did not increase activity (Table 1; Supplementary Figure S4).

To explore the use of other **R2** substituents, we prepared a series of (*R*)-2-amino-dihydropteridinone analogues based on compound **3** having a methyl group in **R1**. Enzyme inhibition assays showed that *n*-butyl (**13**), isopentyl (**14**), 3,3-dimethylallyl (**15**) and 3-methyl-isoxazole (**16**) groups were all tolerated in **R2**, with K_i values for compounds **13**-**16** ranging from 121.1 to 183.2 nM, comparable to the K_i value found for parent compound **3** (194.1 nM) (Table 1, Supplementary Figure S4). Notably, the introduction of a nitrile moiety in **R2** increased the potency of **17** approximately 3-fold (K_i = 66.2 nM) compared to **3** (Table 1, Supplementary Figure S4). These results further suggested that **R2** substituents with *sp*-hybridized orbitals, such as propargyl and nitrile groups, were associated with increased potency. The co-crystal structure of **13** (PDB ID 6CSW; Figure 4B; Supplementary Table S3) bound to VRK1 also confirmed the ligand adopted the canonical binding pose. This co-structure, along with our enzyme inhibition results, showed that the positively charged pocket formed by Arg133 in the hinge region and residues within VRK1 P-Loop could accommodate **R2** substituents with varying structures, including linear or branched aliphatic chains and heteroaromatic rings.

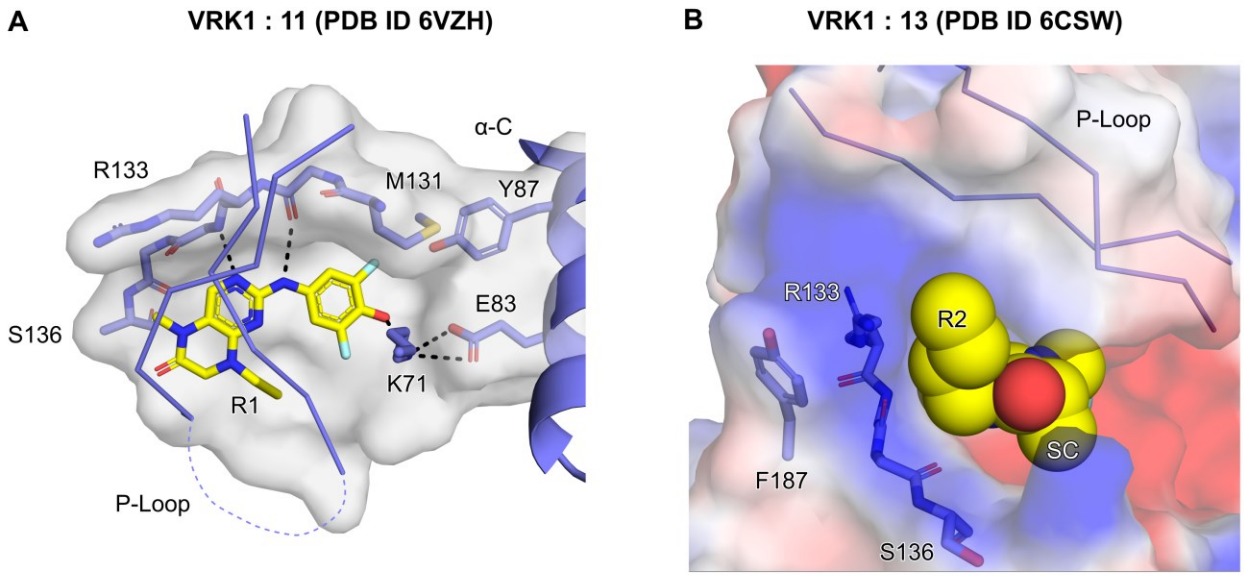

Figure 4. Binding mode of analogues **11** and **13**. (A, B) Co-crystal structure of **11** (A; PDB ID 6VZH) and **13** (B; PDB ID 6CSW) bound to VRK1. Relevant residues and secondary structures around the enzyme ATP-binding site are indicated - α-helix C (blue cartoon), P-Loop (residues 39-55; blue ribbon), the hinge region (residues 132-136; sticks), the gate-keeper residue (M131), the catalytically important glutamate (E83) and lysine (K71) residues, F48 in the P-loop and Y87 in α-helix C. In B, the bottom of VRK1 ATP-binding site is shown as a white (molecular) surface. In B, molecular surfaces are colored by potential (kT/e - calculated by APBS [46] as implemented in PyMOL v. 2.6; red - negative; to blue - positive).

Next, we investigated if the presence of a propargyl in **R1** could improve the potency of (*R*)-2-amino-dihydropteridinone compounds having different moieties in **R2** (Table 2; Supplementary Table S2). To this end, we first replaced the **R1** methyl group in **16** (**R2** = 3-methyl-isoxazole) and **17** (**R2** = acetonitrile) with propargyl. The resulting compounds, **18** (Ki = 26.5 nM) and **19** (Ki = 26.1 nM), were 2- to 5-fold more potent than their counterparts having a methyl group in **R1**. Encouraged by the results, we next prepared three additional (*R*)-2-amino-dihydropteridinone analogues having a propargyl in **R1** and different substituents in **R2** (**20**, **21** and **22**). Our results indicated that increasing the size of the aliphatic chain in **R2** from a methyl (**11**) to an n-ethyl (**20**; Ki = 62.2 nM) led to a 2-fold gain in potency. In line with this observation, substituting the methyl group in the isoxazole motif of **18** with an *H* resulted in a 3-fold potency drop (**21**; Ki = 80.9 nM). We also obtained the co-crystal structure of VRK1 bound to **21** (PDB ID 8V42; Figure 5; Supplementary Table S3). This co-structure confirmed the compound adopted the canonical binding mode and indicated that the ligand isoxazole ring made polar interactions to side chain atoms from Arg133. These results demonstrated that a propargyl group in **R1** improved the potency of (*R*)-2-amino-dihydropteridinone analogues having functionalized groups in **R2**.

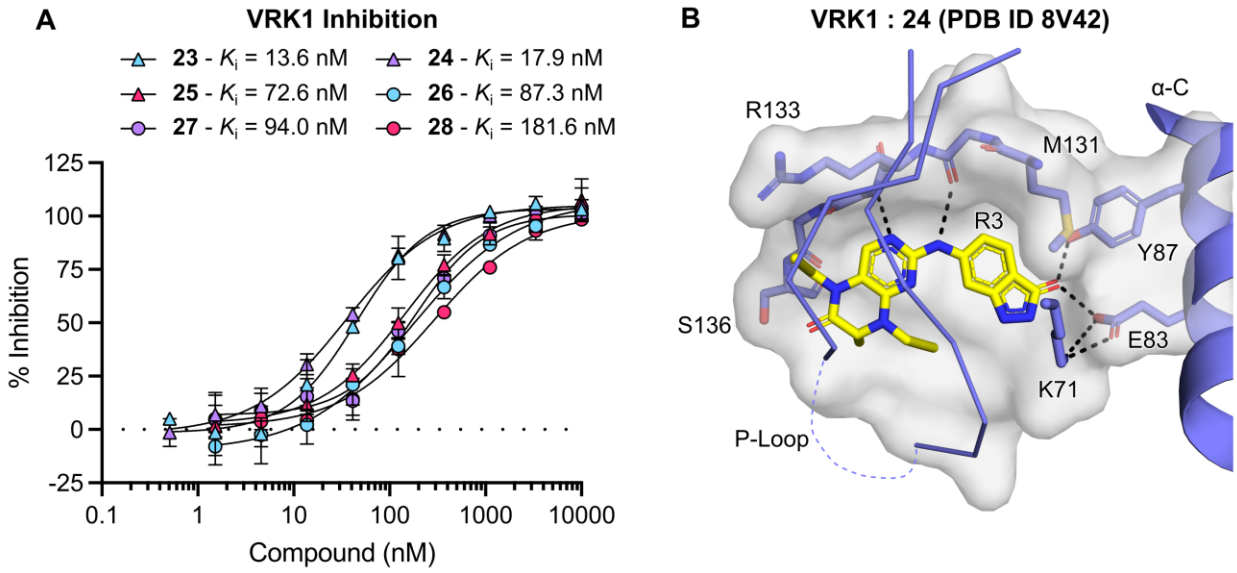

Figure 5. Binding mode of analogue **21**. Co-crystal structure of **21** (PDB ID 8V42) bound to VRK1. Relevant residues in the vicinity of the enzyme ATP-binding site are indicated. Dashed lines indicate potential hydrogen bonds. Molecular surfaces are colored by potential (kT/e - calculated by APBS [46] as implemented in PyMOL v. 2.6; red - negative; to blue - positive).

Table 2 - Structure and activity of (*R*)-pteridinone derivatives having simultaneous changes in R1 and R2

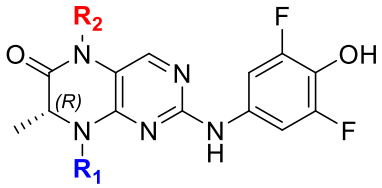

Entry	R1	R2	Ki (nM)[a]
18	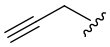	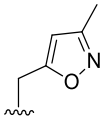	26.5 (19.3 - 36.3)
19	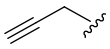	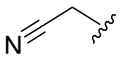	26.1 (22.5 - 30.2)
20	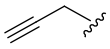		62.2 (5.9 - 653.1)
21	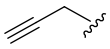	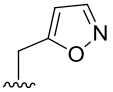	80.9 (69 - 94.6)
22	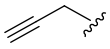	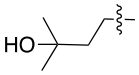	104.7 (45 - 244.3)

[a] inhibition constants calculated using the Cheng-Prusoff equation from IC_{50} values estimated from two independent experiments performed in duplicates; numbers in parenthesis are CI 90%.

Analysis of the co-crystal structures of VRK1 bound to various (*R*)-2-amino-dihydropteridinone analogues revealed the presence of a structural water mediating extensive hydrogen bond interactions between the ligands' difluorophenol moiety (**R3** position) and side chain atoms of two catalytically important and structurally conserved amino acid residues: Lys71 and Glu83, and the less conserved Tyr87 (Figure 2C). To increase compound potency, we used a computational approach to identify novel **R3** moieties that could replace this structural water molecule. *In silico*, we replaced the difluorophenol moiety in **7** with over 5,000 different commercially available **R3** moieties that were compatible with the chemical route used to generate BI-D1870 analogues (see Methods). From the *in silico* evaluations, we selected 12 analogues for synthesis based on their docking scores and by visual inspection of their potential for hydrogen bonding with Glu83 and Tyr87 in VRK1's α-helix C. These selected 12 analogues were tested at a single-point concentration of 1 μM in the VRK1 enzymatic assay. For those with over 85% inhibition, we calculated K_i values from dose-response curves (Table 3). Most analogues were less potent than the parent compound, **7** (Ki = 33.8 nM); however, two indazoles, **23** and **24**, demonstrated 2 to 3-fold greater potency with K_i values of 13.6 nM and 17.9 nM, respectively. These results demonstrated that both amine and hydroxyl groups can act as efficient hydrogen bond donors in **R3**. In contrast, **R3** groups serving as hydrogen bond acceptors such as those in compounds **29**, **30**, **32** and **33**, did not perform well. The co-crystal structure of VRK1 bound to **24** (PDB ID 6NPN) showed the compound's indazole hydroxyl group displaced the structural water and formed similar hydrogen bonds with Lys71, Glu83, and Tyr87 (Figure 6; Supplementary Table S3). These observations suggested that the potency gains for **23** and **24** resulted from an optimized hydrogen bond network facilitated by their **R3** moieties.

Table 3 - Structure and activity of (*R*)-pteridinone derivatives having changes in R3

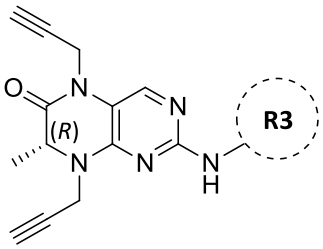

Entry	R3	% inhibition (1 µM) [a]	Ki (nM) [b]
23	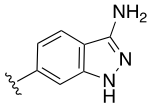	96.8 ± 3.3	13.6 (0.5 - 403.6)
24	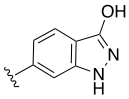	100.7 ± 0.8	17.9 (12.3 - 26.1)
25	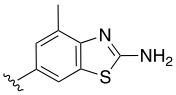	91.5 ± 1.8	72.6 (37.2 - 141.9)
26	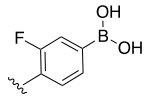	91.6 ± 1.1	87.3 (46.1 - 164.8)
27	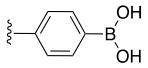	88.5 ± 2.4	94 (79.4 - 111.4)
28	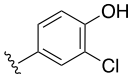	89.6 ± 0.1	181.6 (48.9 - 674.5)
29	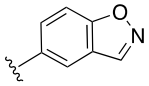	57.4 ± 4.5	ND
30	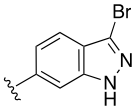	55.7 ± 2.7	ND
31	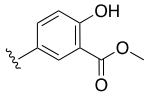	54.1 ± 2.8	ND
32	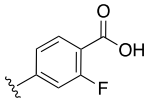	45.2 ± 5.8	ND
33	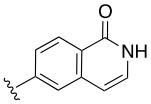	44.4 ± 2.1	ND
34	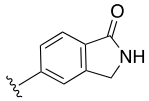	25.1 ± 1.1	ND

[a] values shown are the average ± SD of a single experiment performed in duplicates; [b] inhibition constants calculated using

the Cheng-Prusoff equation from IC_{50} values estimated from two independent experiments performed in duplicates; numbers in parenthesis are CI 90%.; ND - not determined

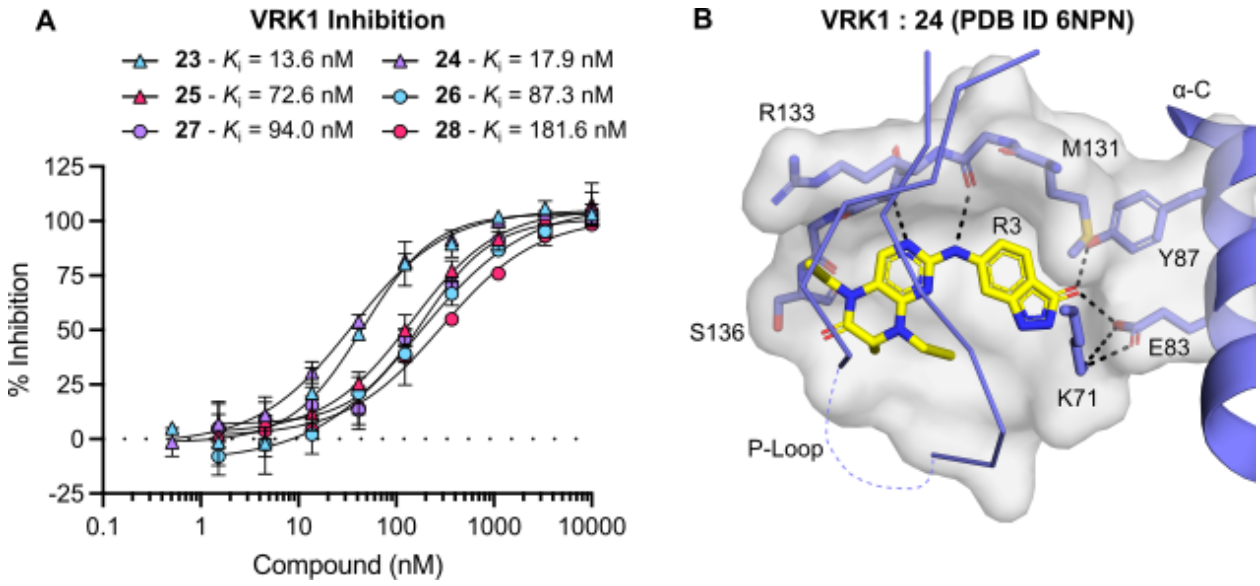

Figure 6. VRK1 inhibition activity of (*R*)-2-amino-dihydropteridinones **23**-**28** and binding mode of analogue **24**. (A) Dose-response curves for analogues **23**-**28**. Data shown are mean ± SD of at least two independent experiments performed in duplicates. Indicated K_i values were obtained by applying the Cheng-Prusoff equation to IC_{50} values determined following fitting of the experimental data to the four-parameter sigmoidal dose-response equation. See Supplementary Table S2 for IC_{50} and SD values. (B) Co-crystal structure of **24** bound to VRK1. Relevant residues and secondary structures around the enzyme ATP-binding site are indicated - α-helix C (blue cartoon), P-Loop (residues 39-55; blue ribbon), the hinge region (residues 132-136; sticks), the gate-keeper residue (M131), the catalytically important glutamate (E83) and lysine (K71) residues, F48 in the P-loop and Y87 in α-helix C. The bottom of VRK1 ATP-binding site is shown as a white (molecular) surface.

In our (*R*)-pteridinone series, compound **1** was 2-fold less potent than racemic BI-D1870, indicating the chiral center's absolute configuration plays an important role in compound efficacy. To investigate this further, we selected seven compounds from the series for re-synthesis with L-alanine as the precursor and then assessed their VRK1 inhibitory activity (Table 4; Supplementary Table S2; Supplementary Figure S5). The activities of these compounds indicated that (*S*)-pteridinones with shorter groups, such as methyl, in **R1** (**35**, **36** and **37**) were up to 5 times more potent than their (*R*)-pteridinone equivalents. In contrast, (*S*)-pteridinones with propargyl moieties in **R1** varied in potency, with some being equivalent (compounds **38** and **39**) and others being 2 to 3 times less potent (compounds **40** and **41**) compared to their (*R*) analogs. These results suggested that the steric effects impacting both (*R*)- and (*S*)-pteridinone scaffolds depended on the identity of the substituents at **R1**.

Table 4 - Structure and activity of (*S*)-pteridinone derivatives having changes in R1, R2 and R3

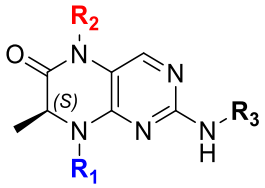

Entry	R1	R2	R3	Ki (nM)[a]
35	Me	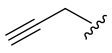	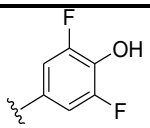	35.2 (28.9 - 42.8)
36	Me	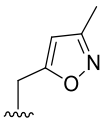	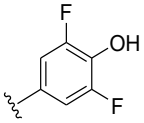	37.9 (24.8 - 58.1)
37	Me	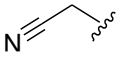	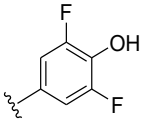	50.0 (17.9 - 139.6)
38	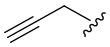	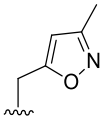	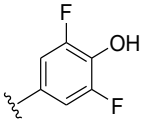	21.8 (13.4 - 35.6)
39	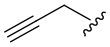	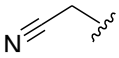	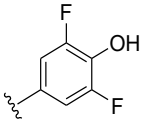	26.1 (16.0 - 42.6)
40	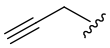	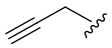	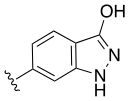	36.9 (7.0 - 193.6)
41	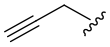	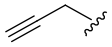	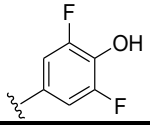	94.2 (63.7 - 139.0)

[a] inhibition constants calculated using the Cheng-Prusoff equation from IC_{50} values estimated from two independent experiments performed in duplicates; numbers in parenthesis are CI 90%.

SELECTIVITY PROFILE OF VRK1 INHIBITORS

We assessed the selectivity of our most promising VRK1 inhibitors by measuring the percentage of enzyme inhibition at a single compound concentration of 1.0 μM across 320 human kinases performed at ProQinase (Table 5; Figure 7 and Supplementary Table S4). Compound **1** exhibited a selectivity index (S_{50}) of 0.114, which reflects the fraction of kinases with less than 50% residual activity. Specifically, kinases with less than 20% residual activity at this concentration were predominantly members of the Ribosomal Protein S6 Kinases (RSK) and Casein Kinases (CK1) families. These findings are consistent with those reported for BI-D1870, a recognized inhibitor of RSK and CK1 kinases. [40] Moreover, these results highlighted the difficulties in creating a selective VRK1 inhibitor from the BI-D1870 pteridinone scaffold.

Nevertheless, our results demonstrated that appropriate modifications to **R1**, **R2**, and **R3** yielded highly selective VRK1 inhibitors. Kinome-wide selectivity data revealed that a smaller substituent in **R1** was crucial for enhancing selectivity. For instance, replacing the isopentyl moiety in **2** (S_{50} = 0.163; K_i = 31.5 nM) with a propargyl (**7**; S_{50} = 0.031; K_i = 33.8 nM) or a cyclopropyl (**8**; S_{50} = 0.044; K_i = 23.1 nM) group markedly increased compound selectivity without affecting compound potency. This pattern was consistent across both (*R*)- and (*S*)-pteridinone series, as evidenced by the high selectivity (S_{50} index range: 0.024 - 0.038) of similarly potent (*S*)-pteridinones with methyl or propargyl substituents in **R1**. Although selectivity improvements were observed when replacing the isopentyl group in **1** and **2** with smaller propargyl or methyl groups, these modifications also reduced potency, thus adding complexity to the analysis. The comparison between matched (*R*)- and (*S*)-pteridinones, particularly **3** and **35**, indicated that the potency increase for the (*S*)-enantiomer did not compromise selectivity, suggesting the chiral center's configuration significantly influenced both attributes. Further experiments are necessary to confirm these findings.

Table 5 - Kinome-wide selectivity profile for selected VRK1 inhibitors

Entry	S_{50}[a]
1	0.114
2	0163
3	0.028
7	0.031
8	0.044
11	0.075
23	0.125
24	0.119
35	0.025
36	0.024
38	0.032
39	0.038

[a] defined as the fraction of kinases tested having < 50 % residual activity

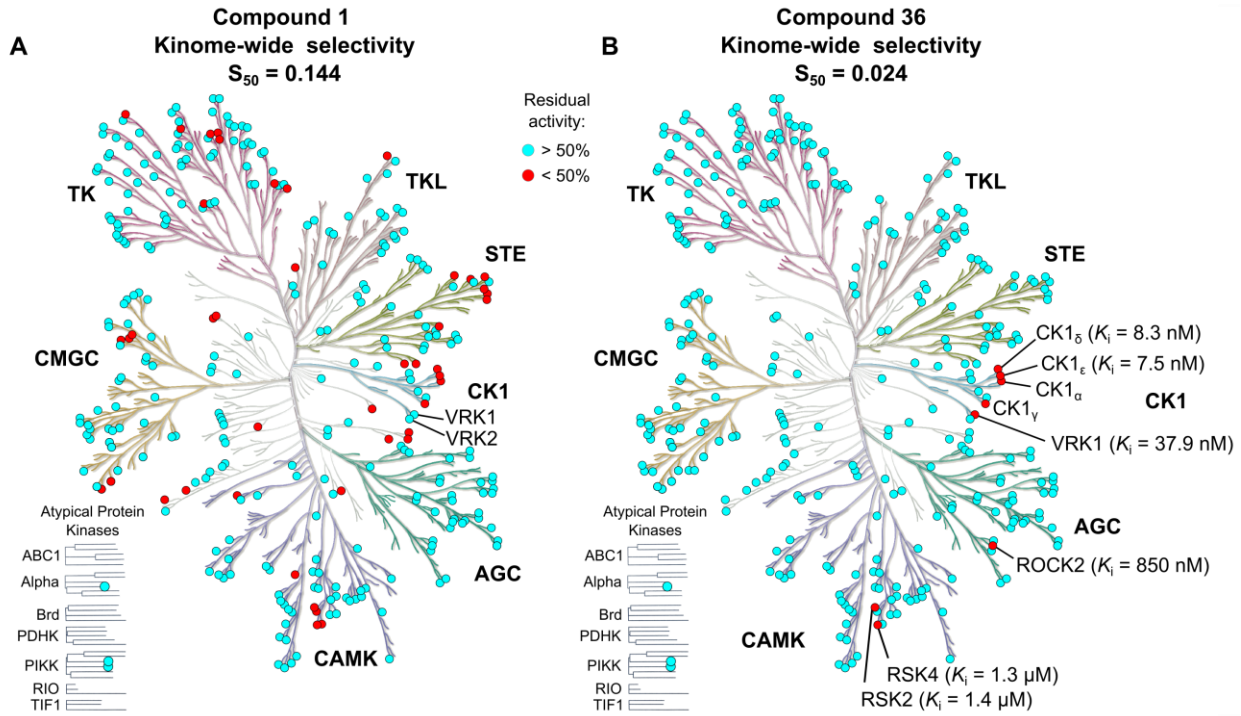

Figure 7 - Human kinome-wide selectivity profiles for compounds **1** and **36**. (A, B) Dendrogram for the human kinome. Colored circles represent tested kinases at 1.0 μM compound. Blue circles > 50% residual activity; red circles ≤ 50% residual activity. Residual activity values were calculated from the average of two independent measurements. In B, numbers in parenthesis are K_i values obtained by applying the Cheng-Prusoff equation to IC_{50} values determined from at least two independent experiments following fitting of the experimental data to the four-parameter sigmoidal dose-response equation.

To complement selectivity data from kinome-wide panels for compound **36**, we determined its K_i values against VRK2 and selected off-targets (Figure 7, Supplementary Figure S6). For VRK2, **36** had an IC_{50} value greater than 3.5 μM, making accurate K_i determination not possible and indicating this compound was markedly less active towards VRK2 compared to BI-D1870 (K_i = 28.0 nM; Supplementary Figure S3E) or **1** (K_i = 17.8 nM; Supplementary Figure S7). Notably, compound **36** demonstrated over 30-fold reduced potency towards two out of six RSK family kinases tested that showed less than 50% residual activity in the kinome-wide selectivity panel. This panel also identified ROCK2 and four Casein Kinases 1 isoforms ($CK1_\alpha$, $CK1_\gamma$, $CK1_\delta$ and $CK1_\varepsilon$) as potential off-targets. Indeed **36** was a potent, single-digit nanomolar inhibitor of $CK1_\delta$ and $CK1_\varepsilon$ (K_i values of 8.3 and 7.8 nM, respectively), whereas the compound was > 20-fold less active towards ROCK2 (K_i = 850 nM) compared to VRK1. Together, these results indicated that **36** is a potent VRK1 inhibitor with few potential off-targets within the human kinome.

Previously, BI-D1870 was shown to interact with Bromodomain-containing (BRD) proteins, which are key in recognizing acetylated lysine residues and recruiting regulatory proteins for chromatin organization. [41,47] Therefore, to verify if **36** could interact with BRD proteins, we employed a thermal-shift assay (Differential Scanning Fluorimetry; DSF), a technique that measures the stabilization of proteins upon ligand binding. [48] Screening against a panel of 32 bromodomains covering all human BRD subfamilies (Supplementary Table S4) revealed that **36** did not produce temperature shifts greater than 0.9 °C. This is below the 2.0 °C threshold commonly used to denote significant ligand binding in the DSF assay. In contrast, BI-D1870 produced temperature shifts greater than 2.0 °C in five BRD proteins. Our DSF selectivity studies thus indicate that **36** has limited interactions with off-target proteins in both the human kinase and BRD protein families, underscoring its specificity.

36 engages VRK1 in live, intact cells

To demonstrate that **36** could permeate intact human cells, we employed a split kinase/split luciferase complementation assay. [49] In this assay, VRK1 was divided into two fragments consisting of residues 1-64 and 65-364. Each fragment, containing a portion of the protein's ATP-binding site, was fused to either the N- or C-terminal part of the *Renilla* luciferase (Figure 8A). The assay is based on the premise that strong ligand binding within the ATP-binding site will bring the kinase fragments together, thus reconstituting both the kinase and luciferase activities and resulting in cellular luminescence. This method was previously demonstrated with Lyn kinase and its inhibitor dasatinib [49] (Figure 8B). Similarly, HEK293 cells co-transfected with plasmids for the VRK1 fragments exhibited significantly higher luminescence in the presence of **36** (30 μM) compared to untreated controls or cells treated with the same concentration of **VRK-N**, a structurally similar compound that does not effectively inhibit VRK1. (Supplementary Figure S8).

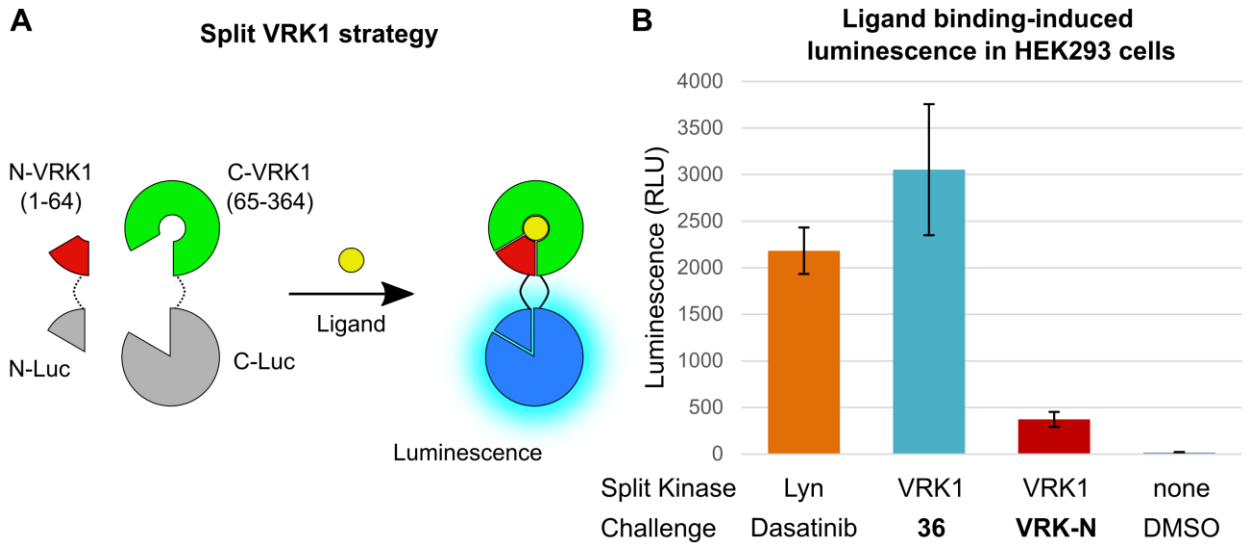

Figure 8 - 36 interacts with VRK1 in live, intact human cells. (A) Split kinase/split luciferase complementation strategy for VRK1. Dashed black lines indicate flexible spacer between individual protein fragments. (B) Light emission by HEK293 cells co-transfected with plasmids encoding N- and C-terminal VRK1/Luciferase fragments and treated with **36** or **VRK-N** - both compounds were added at 30 µM final concentration. HEK293 cells co-transfected with N- and C-terminal Lyn/Luciferase fragments and treated with dasatinib (30 µM final concentration) were used as positive control. Non-transfected cells treated with DMSO only (vehicle) were used as negative control.

Compounds 35 and 36 have improved *in vitro* pharmacokinetics properties compared to BI-D1870

We evaluated the *in vitro* pharmacokinetic profiles of compounds **35** and **36**, examining their aqueous kinetic solubility, distribution coefficients (LogD), metabolic stability, and cytochrome P450 inhibition (Table 6). [50] The same properties were also obtained for BI-D1870. Compounds **35** and **36** displayed notably better pharmacological properties than BI-D1870. Specifically, their solubility in water exceeded 30 µM, a substantial improvement over BI-D1870's solubility of less than 1.6 µM. This enhancement is attributed to the substitution of the isopentyl group in BI-D1870 with a less lipophilic methyl group in **R1** and the addition of polar groups in **R2**, such as propargyl and methyl-isoxazole. Correspondingly, their lower distribution coefficients (LogD = 2.3) indicate improved potential for bioavailability compared to BI-D1870 (LogD = 4.1), with LogD values in the range associated with drug-like molecules. [51]

Additionally, our findings showed that **35** and **36** were more stable in human and mouse microsomes and hepatocytes than BI-D1870, particularly in microsomes where they demonstrated low intrinsic clearance (CL_{int} < 20 µL/min/mg protein) and consequently longer half-lives ($t_{1/2}$ > 30 min). In hepatocytes, however, they exhibited higher intrinsic clearances (CL_{int} > 50 µL/min/106 cells) and shorter half-lives ($t_{1/2}$ < 30 min), suggesting a higher susceptibility to phase II metabolism compared to phase I metabolism. Both compounds also showed no significant inhibition of various cytochrome P450 isoforms (1A2, 2C9, 2C19, 2D6, and 3A) at a concentration of 10 µM, suggesting a low potential for drug-drug interactions or toxicity due to the buildup of harmful metabolites.

Table 6 - *In vitro* pharmacokinetic properties of BI-D1870, 34 and 35			
Parameter	BI-D1870 [a]	**35** [a]	**36** [a]
Aqueous kinetic solubility (µM)	<1.6	39.0 ± 21.9	31.0 ± 19.1
Partition coefficient	4.10 ± 0.18	2.3 ± 0.0	2.3 ± 0.0
Metabolic stability in liver human microsomes	$t_{1/2}$ = 32.2 ± 6.1 [b] CL_{int} = 44.6 ± 8.4 [c]	$t_{1/2}$ = 143.8 ± 1.2 [b] CL_{int} = 9.7 ± 0.1 [c]	$t_{1/2}$ >145 [b] CL_{int} <9.6 [c]
Metabolic stability in liver mice microsomes	$t_{1/2}$ = 20.3 ± 3.1 [b] CL_{int} = 69.9 ± 10.7 [c]	$t_{1/2}$ = 62.1 ± 9.6 [b] CL_{int} = 22.9 ± 3.5 [c]	$t_{1/2}$ = 101.8 ± 12.4 [b] CL_{int} = 13.8 ± 1.7 [c]
Metabolic stability in human liver hepatocytes	$t_{1/2}$ = 7.7 ± 0.2 [b] CL_{int} = 179.9 ± 5.7 [d]	$t_{1/2}$ = 10.9 ± 0.2 [b] CL_{int} = 127.4 ± 2.9 [d]	$t_{1/2}$ = 10.8 ± 1.8 [b] CL_{int} = 132.2 ± 22.7 [d]
Metabolic stability in mice liver hepatocytes [c]	$t_{1/2}$ = 8.4 ± 2.9 [b] CL_{int} = 187.6 ± 64.1 [d]	$t_{1/2}$ = 18.4 ± 9.5 [b] CL_{int} = 102.6 ± 52.8 [d]	$t_{1/2}$ = 21.1 ± 6.2 [b] CL_{int} = 71.8 ± 21.2 [d]
% inhibition of cytochrome P450 activity (10 µM)	1A2 = 56.9 ± 21.0 2C9 = 66.5 ± 13.9 2C19 = 44.4 ± 19.4 2D6 = 13.3 ± 7.2 3A = 10.2 ± 6.2	1A2 = 24.7 ± 2.6 2C9 = 42.8 ± 2.1 2C19 = 54.8 ± 9.5 2D6 = 14.2 ± 4.4 3A = 21.0 ± 6.0	1A2 = 15.1 ± 3.4 2C9 = 23.7 ± 2.8 2C19 = 15.1 ± 10.2 2D6 = 8.7 ± 4.5 3A = 17.5 ± 4.4

[a] values shown are mean ± S.D. from two independent experiments; [b] $t_{1/2}$ - half-life in minutes; [c] CL_{int} - intrinsic clearance in µL/min/mg; [d] CL_{int} in µL/min/10^6 cells.

Pharmacological inhibition of VRK1 leads to cell cycle arrest and genome instability.

Compounds **35** and **36** were tested for their ability to induce cellular phenotypes consistent with VRK1 deficiency, which included examining effects on cell proliferation, genome stability, and interactions with the tumor suppressor p53. [52–54] We first evaluated if the VRK1 inhibitors led to immediate changes in cell proliferation using high-content immunofluorescence imaging of p53-proficient ($p53^{+/+}$) and p53-deficient ($p53^{-/-}$) human retinal pigment epithelial (RPE1) cells following a 24-hour drug exposure. Unlike the negative control, **VRK-N**, both VRK1 inhibitors **35** and **36** triggered a p53-dependent G_0/G_1 phase arrest, with over 80% of the p53-proficient cells arrested in the G_0/G_1 phase after 24 hours of treatment with 15 µM of **36** (Figures 9A, B, and Supplementary Figure S9). By contrast, VRK1-inactive compound **VRK-N** had no impact on the cell cycle.

The selective cytostatic activity of **36** was corroborated using an independent assay based on the redox indicator AlamarBlue [55] (Figures 9C, D). Consistent with the observed p53-dependent cell cycle arrest, **36** upregulated the expression of p53 and its cell cycle target p21 in a dose-dependent manner (Figure 9E). Notably, **36** also reduced the levels of phosphorylated histone H2AX in a dose-dependent manner (Figure 9E), which confirms a role for VRK1 in DNA damage signaling. [56] Treatment of p53-deficient cells with **36** revealed additional signs of compromised genome stability associated with VRK1 deficiency, such as increased micronuclei and abnormal centrosome numbers. [57–59] A three-day treatment with **36** led to a dose-dependent increase in the occurrence of micronuclei (Figures 9F, G) and centrosome abnormalities (Figures 9H, I), particularly in p53-deficient cells. Identical treatment of p53-proficient cells led to a potent cell cycle arrest (Figures 9A, C) and consequent absence of mitotic cells after 3 days of treatment (Figure 9H). Subsequent experiments showed that p53-proficient cells could reverse the cell cycle arrest induced by **36**, implying a potential tolerance for VRK1 inhibition in normal tissues (Supplementary Figure S10). On the other hand, p53-deficient cancer cells are likely to experience persistent genomic instability when subjected to VRK1 inhibition (Figure 9J).

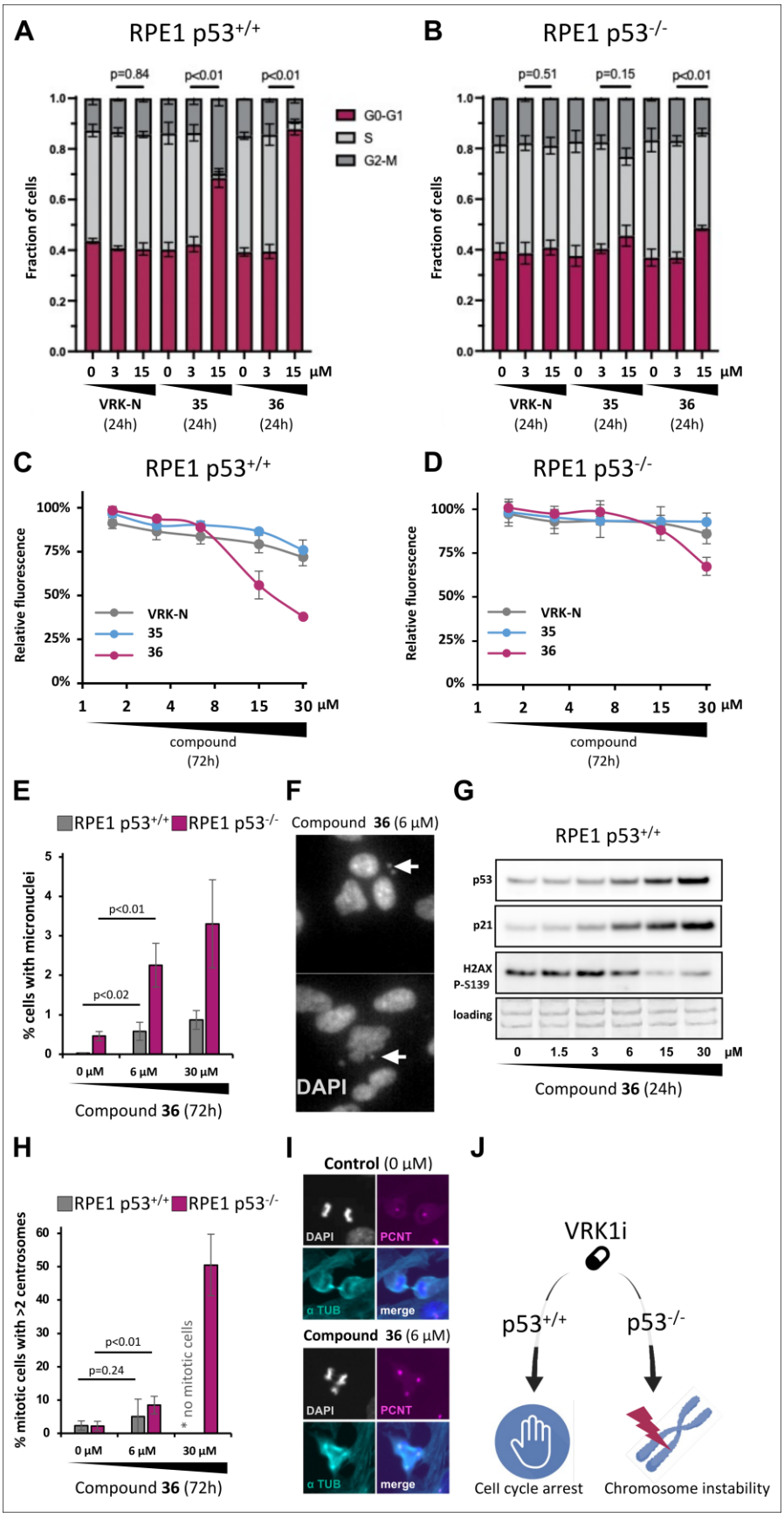

Figure 9 – Pharmacological inhibition of VRK1 causes classic VRK1 deficiency phenotypes including p53-dependent cell cycle arrest and genome instability. (A) Cell cycle distribution of human RPE1 cells upon 24-hour exposure to indicated compound concentrations. Cell cycle status was determined at single cell resolution by high-content microscopy and bar graph depicts mean fractions of three independent experiments. Error bars represent S.E.M., and p values were determined by Welch's t-test (B) Cell cycle distribution of p53-deficient RPE1 cells, performed as in A (C) Relative cellular activity measured by AlamarBlue fluorescence of human RPE1 cell populations exposed to **VRK-N**, **35** or **36** for 3 days. For each compound concentration (x-axis), the mean relative fluorescence intensity of six independent cell populations is depicted (y-axis) and error bars represent SD. Relative fluorescence intensity was determined using mock-treated controls (100%) and negative controls (0%) that were treated with a lethal dose of DMSO. The compound concentrations used, 1.5, 3, 6, 15 and 30 µM, are plotted on a log 2 scale expressed in integers (D) Relative cellular activity of p53-deficient RPE1 cell populations, determined as in C (E) Western blot analysis of human RPE1 cells, exposed to indicated concentrations of **36** for 24 hours. Ponceau-S staining (30-60kDa) is depicted for protein transfer/loading control. (F) Percentage of micronuclei-bearing cells among parental and p53-deficient RPE1 cells after a 3-day **36** treatment. Bar graph depicts mean percentage of six cell populations per compound concentration and error bars represent SD. Welch's t-test indicated significant induction of micronuclei at 6 µM **36** for both cell types (G) DAPI-stained cell nuclei showing nuclear deformations and micronuclei after 6 µM **36** exposure (H) Percentage of cells with abnormal (>2) centrosome foci among parental and p53-deficient RPE1 cells after a 3-day **36** treatment. Bar graph depicts mean percentage of six cell populations per compound concentration and error bars represent SD. Welch's t-test indicated significant induction of centrosome aberrations after 6 µM **36** treatment in p53-deficient cells. (I) Microscopy images of p53-deficient RPE1 cells treated with 0 µM or 6 µM **36**, illustrating the drug-induced multi-polar spindles and ensuing chromosome segregation defects in mitotic cells. Single-channel and merged images are shown for DAPI, PCNT (pericentrin) and α-TUB (α-tubulin). (J) Model highlighting p53-dependent responses to VRK1 inhibitors.

CONCLUSIONS

The lack of suitable chemical tools has limited the validation of VRK1 as a potential therapeutic target. In this study, we detail the structure-based design of novel VRK1 inhibitors based on the pteridinone RSK inhibitor BI-D1870 [38,40]. Our optimized compound, **36**, is as a potent VRK1 inhibitor (Ki = 39 nM) with improved kinome-wide selectivity compared to BI-D1870. Notably, **36** does not bind to bromodomain proteins, a known off-target for BI-D1870, [41] and does not inhibit VRK2, VRK1's closest homologue. The increased selectivity of compound **36** results from targeted modifications at the chiral center and the **R1** and **R2** positions, as our SAR and structural analyses have shown.

Compound **36** engaged with VRK1 in human cells and triggered cell cycle arrest and genome instability, effectively mimicking the effects of VRK1 downregulation using genetic approaches [17,18,22] Notably, these effects were absent with the structurally similar but VRK1-inactive compound, **VRK-N**, underscoring VRK1's crucial role in cell cycle progression and DNA damage response. While p53-proficient cells exhibited reversible cell cycle arrest upon exposure to **36**, indicating a potential for tolerance in normal tissues, p53-deficient cancer cells displayed severe chromosome segregation errors and signs of permanent genomic instability. These findings underscore the significant therapeutic potential of VRK1 inhibitors, particularly for treating p53-deficient tumors, and suggest that combined treatment with VRK1 inhibitors may reduce the required doses of DNA-damaging agents currently in clinical use, such as ionizing radiation and doxorubicin, Olaparib. [14,16,60,61] Similarly, VRK1 inhibition might improve the therapeutic window of potent mitotic drugs such as paclitaxel and Alisertib. [62,63]

Despite these promising results, caution is warranted in applying compound **36** to probe VRK1's cellular functions and therapeutic potential. It is crucial to note that the compound exhibits pronounced activity towards CK1 isoforms. The exact role of these kinases in cell cycle dynamics and DNA repair remains ambiguous; [64] therefore, more rigorous experiments are required to conclusively attribute the cellular effects of **36** to VRK1 inhibition exclusively. Further, a significant potency gap is apparent between the *in vitro* and cellular activities of **36**. This discrepancy may arise from several factors, including VRK2's ability to compensate for VRK1 inhibition in RPE cells, the compound's limited cell permeability, or its reduced efficacy in the ATP-rich intracellular environment.

In conclusion, we expect compound **36** and its negative control **VRK-N** to become invaluable chemical tools to further enhance our understanding of VRK1's role in both normal and disease biology. This study lays a solid foundation for future work aimed at refining the selectivity, cellular efficacy, and metabolic stability of VRK1 inhibitors.

METHODS

Protein Expression and Crystallography

Protein expression and co-crystallization of VRK1 with small molecule inhibitors have been previously reported. [44] Briefly, VRK1 (residues 3-364) was engineered to facilitate crystallization and contained the following surface entropy reduction mutations: K34A/K35A/E36A; E212A/K214A/E215A; E292A/K293A/K295A; and K359A/K360A. For protein production, BL21(DE3)-R3 cells harboring a plasmid expressing lambda phosphatase [65] were cultivated in TB medium supplemented with 50 µg/ml kanamycin and 35 µg/mL chloramphenicol at 37°C until the OD600 reached ~3, and then the temperature was reduced to 18°C for 1 hour. Isopropyl β-D-1-thiogalactopyranoside (IPTG) was added to a final concentration of 0.1 mM, and growth continued at 18°C overnight. Cells were harvested by centrifugation, and the pellets were suspended in 2× lysis buffer (50 mM HEPES, pH 7.5, 500 mM NaCl, 10 mM imidazole, 0.5 mM TCEP, and 1/1000 dilution of Protease Inhibitors Cocktail Set VII - Calbiochem) prior to flash-freezing in liquid nitrogen. After thawing, cells were lysed by sonication on ice. Proteins were purified using Ni-Sepharose resin (GE Healthcare) and eluted stepwise with 300 mM imidazole in the binding buffer. The hexahistidine tags were removed at 4°C overnight using recombinant TEV protease while dialyzing against excess gel filtration buffer (25 mM HEPES, 500 mM NaCl, 0.5 mM TCEP, 5% [v/v] glycerol). Proteins were further purified by reverse affinity chromatography on Ni-Sepharose followed by gel filtration (Superdex 200 16/60, GE Healthcare). The protein in gel filtration buffer was concentrated to 14 mg/ml using 30 kDa MWCO centrifugal concentrators (Millipore) at 4°C. Compounds dissolved in 100% dimethyl sulfoxide (DMSO) were added to the protein solutions at a 3-fold molar excess and incubated on ice for approximately 30 minutes. The mixture was centrifuged at 14,000 rpm for 10 minutes at 4°C before setting up 150-nl volume sitting drops at three ratios of protein-inhibitor complex to reservoir solution (2:1, 1:1, and 1:2). Crystallization experiments were performed at 20°C. Crystals were cryoprotected in reservoir solution supplemented with 20–25% glycerol before flash-freezing in liquid nitrogen for data collection. Diffraction data were collected at the Advanced Photon Source (APS) beamline 24-ID-C and at Diamond Light Source beamline I24. The best diffracting crystals grew under conditions described in Supplementary Table S3. Crystal optimization used Newman's buffer system. [66] Diffraction data were integrated using XDS [67] and scaled using AIMLESS from the CCP4 suite. [68] VRK1 co-crystal structures were determined via molecular replacement with Phaser [69] using the atomic coordinates of the BI-D1870 bound protein (PDB ID 5UVF). [44] Automated refinement was performed with REFMAC5, [70] and manual model

building and refinement were conducted using Coot. [71] Structure validation was carried out using MolProbity. [72] Structure factors and coordinates have been deposited in the Protein DataBank (PDB), as detailed in Supplementary Table S3.

Enzyme Inhibition Assays

TR-FRET-based enzymatic assays for VRK1 and VRK2 were established and performed at WUXI and in-house, respectively. These assays utilized commercially available enzymes obtained from Carna Biosciences (VRK1 cat# 03-110; VRK2 cat# 03-111). Phosphorylation of a fluorescently labeled, generic peptide based on human histone H3 (Perkin Elmer, cat# TRF0125, ARTKQTARKSTGGK; the phosphorylated residue is underlined) by either VRK1 or VRK2 was monitored using commercially available anti-phosphoH3 antibodies labeled with a Europium chelate (Perkin Elmer, cat# TRF0211).

To establish the $K_{M,ATP}$ for VRK2 , the protein and the H3 peptide were diluted in reaction buffer (20 mM HEPES, pH 7.5, 100 mM NaCl, 5 mM $MgCl_2$, 1 mM DTT, and 0.01% Tween 20) to final concentrations of 80 nM and 200 nM, respectively. Then, 5 µL of the diluted protein solution and 2.5 µL of the diluted peptide solution were distributed into a 384-well, round-bottom, white assay plate (Corning, Cat# 4512). Freshly prepared ATP (Sigma, Cat# A7699) dissolved in reaction buffer to a 2 mM concentration was serially diluted (3-fold dilutions, 15 points) in the same buffer, and 2.5 µL from each dilution point was added to the assay plate to initiate the reaction. The final assay concentrations were 40 nM for VRK2 and 50 nM for the H3 peptide. The highest assay concentration of ATP was 500 µM, and the lowest was 110 pM. The plate was incubated for one hour at 30°C, and the enzymatic reaction was stopped by adding 5 µL of 24 mM EDTA in 1X LANCE Detection Buffer (Perkin Elmer, Cat# CR97-100). Subsequently, 5 µL of anti-phosphoH3 antibody (8 nM) in 1X LANCE Detection Buffer was added to each well, and the plate was incubated for 1 hour. TR-FRET measurements were acquired using a CLARIOstar (BMG Labtech) plate reader set to excitation and emission wavelengths of 320 nm and 665 nm, respectively. A LP-TR dichroic filter selective for the 250 to 412 nm reflection and 457 to 900 nm transmission range was used. The assay data were blank-corrected (subtracting the background from all reaction components except the protein) and fitted to Michaelis-Menten kinetics to estimate $K_{M,ATP}$ values in GraphPad Prism (Dotmatics).

To estimate half-maximal inhibitory concentrations (IC_{50}) for test compounds, a 15-point serial dilution (2-fold dilutions) was prepared in 100% DMSO (highest concentration used was 3 mM). VRK2 was diluted in the same reaction buffer used for $K_{M,ATP}$ determination to a concentration of 10 nM, and 5 µL was dispensed into a 384-well, round-bottom, white assay plate (Corning, Cat# 4512). The serially diluted compounds (100 nL) were transferred to the assay plate using an automated liquid handling robot (CyBio

Felix; Analytik Jena) and incubated for 30 minutes at 30°C before the addition of 5 µL of a mixture containing ATP (196 µM) and the H3 peptide (100 nM). The final assay concentrations were 5 nM for VRK2, 98 µM for ATP, and 50 nM for the H3 peptide. Compound concentrations ranged from 30 µM to 1.8 nM. The reaction was incubated for 1 hour at 30°C, and the stop and detection steps were conducted as described for the $K_{M,ATP}$ determination assay. IC_{50} values were obtained by fitting the data to a four-parameter dose-response equation using GraphPad Prism version 8.4 (GraphPad Software, San Diego, California, USA).

Bromodomain Selectivity

Protein expression and purification - A total of 32 bromodomain-containing proteins, covering all BRD subfamilies, were used in the Differential Scanning Fluorimetry (DSF) selectivity panel and were expressed and purified as previously described by Knapp and colleagues. [41,47,73]

Differential Scanning Fluorimetry (DSF) - The assay was performed as previously described. [74] Briefly, recombinant bromodomain-containing proteins were assayed in a 96-well plate at a concentration of 2 µM with 10 µM of the compound in a buffer containing 25 mM HEPES, pH 7.5, 150 mM NaCl, and 0.5 mM TCEP. SYPRO Orange dye (5000× concentrate, Invitrogen) was added at a 1:1000 dilution. Temperature-dependent protein unfolding profiles were measured using an MX3005P real-time qPCR instrument (Agilent Technologies; excitation/emission filters = 492/610 nm), with the temperature increasing at a rate of 3°C/min. Melting temperatures (T_m) were calculated by fitting the fluorescence curves to the Boltzmann equation using GraphPad Prism version 8.4 (GraphPad Software, San Diego, California, USA). Changes in melting temperature upon compound binding are reported as ΔT_m values in °C. Measurements were conducted in triplicate, and average values are presented as ± SD. Data for the bromodomain selectivity panel are included in Supplementary Table S4.

In silico screening / docking

Virtual Nucleophilic Aromatic Substitution (SNAr) or Buchwald-Hartwig coupling reactions were performed by Reactor 18.1.0 (ChemAxon®) using ~5K building blocks (anilines and benzylamines derivatives) in sdf format from the companies Wuxi and Sigma-Aldrich to generate the file of the ligands. In sequence, the computational procedures were carried out by Maestro 11.7 (Schrödinger® 2018; small-molecule drug discovery suite). The 3D structures of the ligands were generated using LigPrep (Epik pH: 7.4±0.5) with partial charges ascribed using OPLS3e force field. The human vaccinia-related kinase protein structure (PDB code: 5UVF; chain C) was prepared using Protein Preparation Wizard (Epik pH: 7.4±0.5 and OPLS3e force field). Water molecules outside of the binding site as well as the structural water at the deep

pocket region (αC helix) were removed. The docking grid was defined by a 20 Å x 20 Å x 20 Å box centered in the central ligand position (co-crystal template). Ligand docking was carried out using Glide containing the following constrained groups: backbone atoms from the hinge residues (Asp132, =O and Phe134, -NH), side chain atoms from structurally-conserved and catalytically-important residues (Lys71, -NH and Glu83, =O) and the atoms from the non-conserved residue Tyr87, -OH. The score value from Glide Emodel and a visual inspection were used to rank the docking poses generated and select compounds for subsequent synthesis at Wuxi.

Cell Biology

Human hTERT-RPE1 cells (hereafter referred to as RPE) were cultured in an ambient-controlled incubator at 37°C with 5% CO_2 and maintained using DMEM-F12 GlutaMAX (Thermo Fisher Scientific, 31331093) supplemented with 1% Pen/Strep (Thermo Fisher Scientific, 15140122) and 10% heat-inactivated FBS (Sigma, F7524). The p53-deficient and isogenic parental RPE cells were kindly provided by Arne Lindqvist [75] and were regularly tested for mycoplasma contamination.

Microscopy and quantitative immunofluorescence. For cell cycle analysis experiments, 7,000 RPE $p53^{+}/^{+}$ and RPE $p53^{-}/^{-}$ cells were seeded in 96-well imaging plates (Sigma) 24 hours before drug treatments. Compounds (**35**, **36**, and **VRK-N**) were dissolved in DMSO to prepare 30 mM stock solutions and added to the medium at the indicated concentrations for 24 hours. EdU (5-ethynyl-2'-deoxyuridine, 10 mM; Jena Bioscience) was added to live cells for 1 hour prior to fixation. Cells were then washed with TBS supplemented with 0.1% Tween-20 (hereafter referred to as TBS/T) and DPBS (#2037539, GIBCO), fixed in a 4% formaldehyde solution (#02176; Histolab) for 7 minutes, permeabilized in cold methanol (Sigma Aldrich) for 2 minutes, washed in TBS/T and DPBS, and incubated in blocking media (TBS/T and 2% bovine serum albumin) for 1 hour. Fixed samples were incubated with the primary antibody (Cyclin A2, 1:400; #66391-1-Ig; Proteintech) in blocking media overnight at 4°C, washed in TBS/T and DPBS, and incubated with the secondary antibody (Alexa Fluor 555-Goat anti-Mouse, 1:800, #A21422, Life Technologies) and DAPI (100 ng/ml; #D1306; Thermo Fisher Scientific) for 1 hour at room temperature. Samples were then washed in TBS/T and DPBS, and EdU-Click chemistry was performed by incubation in 100 mM Tris, 1 mM $CuSO_4$ (C1297; Sigma), 100 mM ascorbic acid (#A4544, Sigma), and fluorescent dye azide (#A10277, Invitrogen) for 1 hour at room temperature, followed by washing in TBS/T and DPBS. Stained samples were stored in DPBS. Images were acquired at room temperature using a Nikon Ti2 ECLIPSE microscope with a 20X air objective and analyzed using CellProfiler and custom R pipelines. To assess cell cycle stages from high-content IF data, nuclei were segmented in CellProfiler using Global Otsu thresholding.

Integrated intensities for DAPI, EdU, and Cyclin A2 signals were obtained for each nucleus. Nuclear signal intensities were normalized relative to the baseline G1 cell population (EdU-negative/low DAPI) and classified into G1, S, G2, and M phases based on nuclear intensities of Cyclin A2, EdU, and DAPI using hard-coded line boundaries (Supplementary Figure S8). Micronuclei and centrosome analyses were performed as described above, except cells were treated with compound **36** at the indicated concentrations. Fixed samples were treated with primary antibodies against Tubulin (α, 1:400; #T9026; Sigma), Pericentrin (1:400; #ab4448; Abcam), and the corresponding secondary antibodies Alexa Fluor 555-Goat anti-Mouse (1:800, #A21422, Life Technologies) and Alexa Fluor 488-Goat anti-Rabbit (1:800, #A11008, Life Technologies), followed by DAPI staining. Images were acquired as above and analyzed with CellProfiler to count the total cell number and by manual counting of micronuclei and centrosomes (over 2500 nuclei per condition, in sextuplicate).

Cellular metabolism assay. Cellular activity was assessed using the alamarBlue cell viability assay (#BUF012, Bio-Rad). A total of 1,000 RPE $p53^{+}/^{+}$ and RPE $p53^{-}/^{-}$ cells were seeded in 96-well imaging plates (Sigma) 24 hours before drug treatments. Compounds **35**, **36**, and **VRK-N** were added to the medium at the indicated concentrations for 72 hours. Each analysis plate included six baseline controls treated with a lethal dose of 10% DMSO to nullify viability. A 10% volume of the cell viability reagent was added directly to the cells in culture medium and incubated for 4 hours. Emitted fluorescence was measured at a wavelength of 600 nm using a Tecan Infinite M200 Pro plate reader, and data were analyzed using Tecan i-control software. Cell viability was expressed relative to the negative controls (10% DMSO-treated) and mock-treated positive controls. For studying drug recovery, the cellular metabolism assay was conducted as described above, except that cells were treated with **36** at a 30 µM concentration for 72 hours, then washed and allowed to recover for 3 days in fresh media without the drug. Viability was assessed either immediately following the 72-hour treatment (control samples) or after the 3-day recovery period (reversibility samples).

Western blot. For protein expression analysis, 600,000 RPE $p53^{+}/^{+}$ cells were seeded in 6-well culturing plates (Sarstedt) 24 hours before inhibitor treatments. Compound **36**\ was added to the medium at concentrations of 0 µM, 1.5 µM, 3 µM, 6 µM, 15 µM, and 30 µM for 24 hours. Cells were washed with DPBS (D8537; Gibco) and lysed in RIPA buffer (#89901; Thermo Fisher Scientific) supplemented with protease inhibitors (Complete ULTRA; Roche) and phosphatase inhibitors (PhosSTOP; Roche), and then sonicated for three cycles of 30 seconds on and 30 seconds off in a Bioruptor® (Diagenode). Protein concentrations were quantified using the DC™ Protein Assay Kit II (#5000112; Bio-Rad) and samples were

denatured at 70°C for 10 minutes using NuPAGE LDS Sample Buffer (#NP0008; Invitrogen) and NuPAGE Reducing Agent (#NP0004; Invitrogen). Gel electrophoresis was performed using NuPAGE 4 to 12% Bis-Tris Protein Gels (NP0321; Invitrogen) and proteins were transferred onto a nitrocellulose membrane using the Trans-Blot Turbo RTA Mini 0.2 µm Nitrocellulose Transfer Kit (#1704270; Bio-Rad). The membrane was blocked in TBS/T containing 5% skim milk and probed with primary antibodies (α-p53 #ab1101, Abcam; α-p21 #2947T, CST; α-H2AX pS139 #05-636, Merck; or α-vinculin #ab129002, Abcam) and HRP-conjugated secondary antibodies (α-mouse #A9044; Sigma or α-rabbit #A6154; Sigma). Chemiluminescence signals were detected using SuperSignal™ West Dura Extended Duration Substrate (#34076; Thermo Fisher Scientific) and imaged with an Amersham Imager 600.

Split-kinase assay. In-cell target engagement assays were performed using a split kinase/luciferase assay as previously described. [49] Briefly, the synthetic DNA sequence encoding the N-terminal fragment of the VRK1 kinase domain (residues 1–64), a 10-amino acid flexible linker (sequence: GGSGGGSGGS), and the C-terminal fragment of Firefly Green Fluorescent Protein (UniProt ID P08659; residues 491–547) were introduced into the mammalian expression vector pTwist CMV to generate VRK1-Nter-64. Similarly, the sequence for the N-terminal fragment of Firefly Green Fluorescent Protein (UniProt ID P08659; residues 2–491), a 10-amino acid flexible linker (sequence: GGSGGGSGGS), and the C-terminal fragment of the VRK1 kinase domain (residues 65–364) were cloned into the same vector to generate the plasmid VRK1-Cter-68. The constructs used for the split Lyn kinase/luciferase were described previously. [49] For VRK1, the splitting point was determined based on the crystal structure and the published work on the Lyn protein kinase. [49] HEK293 cells were maintained in DMEM media (Gibco, Thermo Fisher Scientific) supplemented with 10% fetal bovine serum (Seradigm, Avantor) and cultured at 37°C with 5% CO2. For in-cell target engagement assays, both plasmids were co-transfected into HEK293 cells using Lipofectamine LTX with PLUS reagent (Invitrogen, USA) in 6-well plates for 24 hours. Co-transfected cells were then plated at 25,000 cells/well on 96-well OPTI-Plates for 3 hours before the addition of the compound. Cells were incubated with the compound for 40 minutes before the addition of D-luciferin (Promega). Final assay concentrations were as follows: compounds at 30 µM, D-luciferin at 0.3 mM, and vehicle (DMSO) at 1.5%. After a 5-minute incubation, luminescence was measured every 30 seconds using a Varioskan LUX plate reader (Thermo Fisher Scientific) with SkanIt® software.

Pharmacokinetics

Distribution Coefficient Assay: The distribution coefficient (logD) was determined in n-octanol/aqueous phosphate buffer (100 mM, pH 7.4) using the shake-flask method. Compounds were incubated for 1 hour,

with two independent determinations performed in duplicate, under constant shaking (880 rpm) at room temperature. After incubation, samples from each layer were analyzed by HPLC-MS/MS. LogD was calculated as the log10 of the ratio of the compound's concentration in the organic phase to that in the aqueous phase.

Aqueous Kinetic Solubility: Aqueous solubility was measured in phosphate-buffered saline (PBS, pH 7.4) using the shake-flask method. Compounds were diluted in DMSO and transferred to the assay medium. Samples were incubated at room temperature for 24 hours, with two independent determinations performed in duplicate, and analyzed by HPLC-UV/VIS. Aqueous solubility was calculated as the ratio of the peak area from the test sample to that of a calibration standard (60% methanol and 40% water). Solubility results exceeding the maximum assay concentration were reported as >200 µM.

Metabolic Stability in Liver Microsomes: Microsomal metabolic stability was assessed using human liver microsomes (HLM). Compounds (100 nM) were incubated with HLM (0.1 mg protein/mL) at 37°C, with one set of determinations conducted in duplicate for 0, 15, 30, 45, and 60 minutes. Samples were analyzed by HPLC-MS/MS. The in vitro half-life ($t_{1/2}$) and microsomal intrinsic clearance (CL_{int}) for each compound were calculated from the disappearance rate (k, the slope of the natural log of concentration versus time curve), assuming first-order kinetics, using the formulas $t_{1/2} = 0.693/-k$ and $CL_{int} = 0.693/t1/2 \times$ microsomal protein concentration.

Metabolic Stability in Liver Hepatocytes: Hepatocyte metabolic stability was evaluated using CD-1 mouse and human cryopreserved hepatocytes. Compounds (1 µM) were incubated with hepatocytes (0.7×10^6 viable cells/mL) at 37°C for 0, 0.5, 1, 1.5, and 2 hours. Both human and mouse hepatocyte stability assays were performed as two independent determinations in duplicate. Samples were analyzed by HPLC-MS/MS. The in vitro half-life ($t_{1/2}$) and hepatic intrinsic clearance (CL_{int}) of each compound were calculated based on their disappearance rate (k) and assuming first-order kinetics, using the formulas $t_{1/2} = 0.693/-k$ and $CL_{int} = 0.693/t_{1/2} \times$ number of cells per µL.

Cytochrome P450 (CYP) Inhibition: CYP inhibition assays were conducted for isoforms 1A2, 2C9, 2C19, 2D6, and 3A4 using recombinant human enzymes and fluorometric quantification. Compounds (10 µM) were incubated for 20 to 50 minutes, once in duplicate, at 37°C with each isoform and specific substrates. The substrates used were 7-methoxy-4-trifluoromethylcoumarin for 2C9 and 2D6, 3-cyano-7-ethoxycoumarin for CYP1A2 and 2C19, 7-benzyloxy-4-trifluoromethylcoumarin, and benzyloxyresorufin for 3A4.

Chemistry

All chemicals and solvents of analytical grade were obtained from commercial sources and used as received without further purification. Analytical thin-layer chromatography (TLC) was performed on pre-coated silica gel 60 F254 aluminum plates (Merck) with visualization under UV light at 254 nm and 360 nm. High-resolution mass spectra (HRMS) were recorded on an Agilent Q-TOF instrument. ESI mass spectra were acquired on an Agilent LC-MS. ^{1}H and ^{13}C NMR spectra were recorded at 400 MHz and 500 MHz, respectively, on a Bruker Avance instrument using DMSO-d6 and CD3OD as solvents. Chemical shifts were referenced to the residual non-deuterated solvent signals or to tetramethylsilane (TMS) as an internal standard. Coupling constants (*J*) are reported in Hertz (Hz) with multiplicities designated as s (singlet), bs (broad singlet), d (doublet), t (triplet), dd (doublet of doublets), td (triplet of doublets), q (quartet), quint (quintet), and m (multiplet). All assayed compounds had purity ≥95% (for further details see Supporting Information).

Preparation of L/D Amino Acid Methyl Ester Hydrochloride (ii): Methanol was cooled in a round-bottom flask set in an ice bath. Thionyl chloride (0.3 mL/mmol) was added to the methanol, and the mixture was stirred at 0°C for 15 minutes. L/D-amino acid (1 eq) was then added, and the reaction mixture was left stirring at room temperature overnight. After 16 hours, volatiles were removed under reduced pressure.

Preparation of Nitropyrimidine Derivatives (Step 1): L/D-amino acid methyl ester hydrochloride (ii) (1.1 eq) was dissolved in distilled water (4 mL/mmol) in a round-bottom flask. To this solution, 2,4-dichloro-5-nitropyrimidine (**1**-**41**) or 2,4-dichloro-5-nitro-6-methylpyrimidine (**42**, **VRK-N**) (1 eq) was added, followed by diethyl ether (4 mL/mmol) and K_2CO_3 (3 eq). The reaction mixture was stirred overnight at room temperature. Upon completion, the mixture was poured into a 2N HCl solution, and the reaction was extracted with ethyl acetate. The organic phases were collected, dried over anhydrous sodium sulfate, and concentrated under reduced pressure. The crude material was used in the next step without further purification.

Reduction to Obtain Dihydro-5H-Pteridin-6-one Derivatives (iii) (Step 2): The crude material from the previous step (1 eq) was dissolved in acetic acid (AcOH) (5 mL/mmol) in a round-bottom flask. Iron powder (0.5 g/mmol) was added in portions with caution due to the exothermic reaction. The mixture was stirred overnight at room temperature. The resulting reddish solid was filtered under reduced pressure and the filtrate was evaporated. Cold distilled water was added to the residue to precipitate the solid, which was then filtered and dried in the air. This material was used in the subsequent step without further purification.

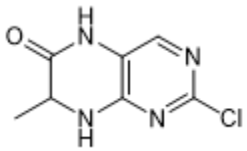

(*R*)/(S)-2-chloro-7-methyl-5,6,7,8-tetrahydropteridin-6-one. Off-white solid**.** **^{1}H NMR (400MHz, DMSO-d_6)** δ = 10.62 (br s, 1 H), 8.47 (s, 1 H), 7.52 (s, 1 H), 4.25 (q, *J* = 6.6 Hz, 1 H), 1.36 (d, *J* = 6.8 Hz, 3 H). MS [M+H]: 199.1. **Yield** = 90% (2.5g).

***N*-Alkylation Reaction to Generate iv**: In a round-bottom flask, the pteridinone derivative (1 eq) was dissolved in DMF (1.5 mL per 100 mg), and the flask was placed in an ice bath. Sodium hydride (NaH) 60% in mineral oil (1.25 eq) was added in small portions. After the addition of all NaH, the reaction mixture was stirred at 0°C for 15 minutes. Subsequently, the alkyl bromide (1.25 eq) was added in one portion, and the reaction was left stirring at room temperature for an additional hour. Following the reaction time, as monitored by TLC analysis, the reaction mixture was poured into distilled water, acidified with 2N HCl solution, and extracted with ethyl acetate. The organic phases were collected, washed with brine, dried over anhydrous sodium sulfate, and the volatiles were removed under reduced pressure. The crude material was purified by silica gel chromatography using a 60-30% hexane:ethyl acetate (Hex:EtOAc) gradient as the eluent.

Synthesis of (*R*)/(*S*)-Pteridinone Derivatives 1-42: In a vial, **iv** (1 eq) was suspended in 80% ethanol (EtOH) (0.5 mL per 30 mg). The aniline derivative (1.1 eq) was added, followed by one drop of HCl per 50 mg of the reaction mixture. The mixture was left stirring at 110°C overnight. Upon completion of the reaction, as indicated by TLC analysis, all volatiles were removed under reduced pressure. The crude material was purified by silica gel chromatography using 10% methanol:ethyl acetate (MeOH:EtOAc) as the eluent.

(*R*)-2-(3,5-Difluoro-4-hydroxy-phenylamino)-5,7-dimethyl-8-(3-methyl-butyl)-7,8-dihydro-5*H*-pteridin-6-one (1) grey solid. ^{1}H NMR (400MHz, DMSO-d6): δ 10.18 (bs, 1H), 9.97 (bs, 1H), 7.73 (s, 1H), 7.27-7.25 (d, *J* = 9.27Hz, 2H), 4.46-4.42 (q, *J* = 6.60Hz, 1H), 3.89-3.83 (m, 1H), 3.18 (s, 3H), 1.61-1.55 (m, 2H), 1.47-1.43 (m, 1H), 1.42-1.40 (d, *J* = 6.92Hz, 3H), 0.88-0.85 (t, *J* = 6.45Hz, 6H). ^{13}C NMR (100MHz, DMSO-d6): δ 163.4, 153.0, 152.9, 151.2, 151.2, 151.1, 151.0, 150.4, 129.7, 126.2, 115.2, 105.1, 56.5, 44.8, 35.0, 28.1, 25.8, 22.3, 22.1, 18.4. MS [M+H]: *m/z* 392.2. Yield = 57% (55mg).

(*R*)-2-(3,5-Difluoro-4-hydroxy-phenylamino)-7-methyl-8-(3-methyl-butyl)-5-prop-2-ynyl-7,8-dihydro-5*H*-pteridin-6-one (2) light brown solid. ^{1}H NMR (400MHz, DMSO-d_6): δ 10.23 (bs, 1H), 10.01 (bs, 1H), 7.78

(s, 1H), 7.27-7.25 (d, *J* = 9.27Hz, 2H), 4.72-4.64 (m, 2H), 4.52-4.49 (q, *J* = 6.60Hz, 1H), 3.09-3.04 (m, 2H), 1.63-1.55 (m, 2H), 1.42-1.40 (d, *J* = 6.76Hz, 3H), 1.20-1.17 (t, *J* = 7.23Hz, 2H), 0.87-0.85 (t, *J* = 5.8Hz, 6H). ^{13}C NMR (100MHz, DMSO-d6): δ 163.0, 153.0, 151.5, 151.1, 113.0, 77.4, 75.6, 67.1, 56.5, 45.5, 45.0, 35.0, 30.4, 25.9, 22.3, 18.3, 8.5. MS [M+H]: *m/z* 416.1. Yield = 37% (13mg).

***(R)*-2-(3,5-Difluoro-4-hydroxy-phenylamino)-7,8-dimethyl-5-prop-2-ynyl-7,8-dihydro-5*H*-pteridin-6-one (3)** beige solid. ^{1}H NMR (400MHz, DMSO-d6): δ10.44 (bs, 1H), 10.05 (bs, 1H), 7.77 (s, 1H), 7.32-7.30 (d, *J* = 9.43Hz, 2H), 4.74-4.64 (ddd, *J* = 15.5 HZ/ 10.85Hz/ 8.49Hz/ 2.36Hz, 2H), 4.54-4.50 (q, *J* = 6.92Hz, 1H), 3.41-3.40 (t, *J* = 2.36Hz, 1H), 3.15 (s, 3H), 1.43-1.41 (d, *J* = 6.92Hz, 3H). ^{13}C NMR (100MHz, DMSO-d6): δ 162.9, 153.0, 152.9, 151.7, 151.1, 113.0, 105.3, 105.1, 77.3, 75.6, 57.9, 33.6, 30.3, 17.5. MS [M+H]: *m/z* 360.1. Yield = 44% (35mg).

(*R*)-2-((3,5-difluoro-4-hydroxyphenyl)-amino)-8-ethyl-7-methyl-5-(prop-2-yn-1-yl)-7,8-dihydropteridin-6(5H)-one (4) off-white solid. ^{1}H NMR (400MHz, DMSO-d6): δ 10.20 (bs, 1H), 9.98 (bs, 1H), 7.76 (s, 1H), 7.32-7.29 (d, J = 9.17Hz, 2H), 4.68 (s, 2H), 4.57-4.52 (q, J = 5.62Hz, 1H), 3.85-3.80 (q, J = 6.85Hz, 1H), 3.39 (s, 1H), 1.43-1.41 (d, J = 6.85Hz, 3H), 1.24-1.21 (t, J = 6.85Hz, 3H). MS [M+H]: *m/z* 374.1. Yield = 42% (10mg).

(*R*)-2-(3,5-Difluoro-4-hydroxy-phenylamino)-7-methyl-8-propyl-5-prop-2-ynyl-7,8-dihydro-5*H*-pteridin-6-one (5) off-white solid. ^{1}H NMR (400MHz, DMSO-d6): δ 9.83 (bs, 1H), 9.67 (bs, 1H), 7.94 (s, 1H), 7.45 – 7.43 (d, J = 9,9Hz, 2H), 4.51-4.46 (m, 2H), 4.36 – 4.33 (d, J = 17,13Hz, 1H), 3.84 – 3.79 (m, 1H), 3.76 – 3.71 (m, 1H), 3.36 (s, 1H), 1.57 – 1.52 (q, J = 7,23Hz, 2H), 1.43 – 1.41 (d, J = 6,76Hz, 3H), 0.89 – 0.86 (t, J = 7,23Hz, 3H). ^{13}C NMR (100MHz, DMSO-d6): δ 163.4, 153.1, 153.0, 150.8, 113.7, 103.2, 78.8, 75.3, 56.8, 41.9, 35.2, 21.0, 19.3, 17.4, 10.9. MS [M+H]: *m/z* 388.2. Yield = 55% (15mg).

(*R*)-8-Allyl-2-(3,5-difluoro-4-hydroxy-phenylamino)-7-methyl-5-prop-2-ynyl-7,8-dihydro-5*H*-pteridin-6-one (6) beige solid. ^{1}H NMR (400MHz, DMSO-d6): δ 10.25 (s, 1H), 9.94 (bs, 1H), 7.84 (s, 1H), 7.31-7.29 (d, *J* = 9.05Hz, 2H), 5.97-5.89 (m, 1H), 5.34-5.30 (d, *J* = 17.2Hz, 1H), 5.26-5.23 (d, *J* = 10.15Hz, 1H), 4.70 (s, 2H), 4.47-4.41 (m, 1H), 4.12-4.07 (m, 1H), 3.40 (s, 1H), 1.42-1.41 (d, *J* = 6.36Hz, 3H). ^{13}C NMR (100MHz, DMSO-d6): δ 163.0, 151.4, 150.9, 132.1, 118.3, 113.0, 77.4, 75.6, 56.5, 48.4, 30.4, 18.1. MS [M+H]: *m/z* 386.1. Yield = 71% (35mg).

(*R*)-2-(3,5-Difluoro-4-hydroxy-phenylamino)-7-methyl-5,8-di-prop-2-ynyl-7,8-dihydro-5*H*-pteridin-6-one (7) off-white solid. ^{1}H NMR (400MHz, DMSO-d6): δ 10.29 (bs, 1H), 9.82 (bs, 1H), 7.90 (s, 1H), 7.42-7.40 (d, *J* = 9.29Hz, 2H), 4.70 (s, 2H), 4.62-4.59 (m, 1H), 4.50-4.38 (m, 2H), 3.40-3.38 (d, *J* = 8.68Hz, 2H),

1.48-1.47 (d, *J* = 6.60Hz, 3H). ^{13}C NMR (100MHz, DMSO-d6): δ 162.8, 153.3, 151.1, 113.0, 104.4, 78.4, 77.4, 75.5, 57.0, 35.8, 30.4, 17.8. MS [M+H]: *m/z* 384.0. Yield = 54% (25mg).

***(R)-8-(cyclopropylmethyl)-2-((3,5-difluoro-4-hydroxyphenyl)-amino)-7-methyl-5-(prop-2-yn-1-yl)-7,8-dihydropteridin-6(5H)-one* (8)** beige solid. ^{1}H NMR (500 MHz, CD3OH) δ 7.88 (s, 1H), 7.29 (d, J = 10.5 Hz, 2H), 4.82 (dd, J = 11.5, 2.4 Hz, 1H), 4.62 (dd, J = 17.7, 2.4 Hz, 1H), 4.45 (q, J = 6.8 Hz, 1H), 3.85 (dd, J = 14.3, 6.9 Hz, 1H), 3.26 (dd, J = 14.3, 6.8 Hz, 1H), 2.77 (t, J = 2.4 Hz, 1H), 1.40 (d, J = 6.8 Hz, 3H), 1.23 (dd, J = 12.2, 6.0 Hz, 1H), 0.64 (dt, J = 8.1, 3.9 Hz, 1H), 0.58 (dd, J = 8.6, 4.5 Hz, 1H), 0.39 (dd, J = 9.2, 4.3 Hz, 1H), 0.34 (dd, J = 9.2, 4.2 Hz, 1H). ^{13}C NMR (126 MHz, CD3OH) δ 165.92, 157.34, 152.95, 139.89, 133.91, 129.27, 114.16, 103.88, 103.81, 103.73, 103.67, 78.30, 74.20, 58.01, 50.72, 31.36, 30.67, 17.22, 10.26, 4.70, 4.06. MS [M+H]: m/z 400.2. Yield = 42% (18mg).

***(R)*-2-(3,5-Difluoro-4-hydroxy-phenylamino)-5,7-dimethyl-8-propyl-7,8-dihydro-5*H*-pteridin-6-one (9)** beige solid. ^{1}H NMR (400MHz, DMSO-d6): δ 10.01 (bs, 1H), 9.83 (bs, 1H), 7.75 (s, 1H), 7.34-7.32 (d, *J* = 9.59Hz, 2H), 4.43-4.39 (q, *J* = 6.44Hz, 1H), 3.79-3.74 (m, 1H), 3.27-3.22 (m, 1H), 3.19 (s, 3H), 1.74-1.68 (m, 1H), 1.65-1.59 (m, 1H), 1.39-1.37 (d, *J* = 6.6Hz, 3H), 0.91-0.88 (t, *J* = 7.3Hz, 3H). ^{13}C NMR (100MHz, DMSO-d6): δ 163.5, 153.0, 152.9, 151.1, 151.0, 150.9, 114.9, 103.8, 103.6, 56.7, 47.5, 28.0, 19.8, 18.2, 10.9. MS [M+H]: *m/z* 364.2. Yield = 39% (60mg).

***(R)*-8-allyl-2-((3,5-difluoro-4-hydroxyphenyl)-amino)-5,7-dimethyl-7,8-dihydropteridin-6(5H)-one (10)** beige solid. **^{1}H NMR (400 MHz, DMSO)** δ 10.43 (s, 1H), 10.01 (s, 1H), 7.77 (s, 1H), 7.27 (d, J = 9.5 Hz, 2H), 5.91 (ddt, J = 16.0, 10.6, 5.5 Hz, 1H), 5.32 (d, J = 17.1 Hz, 1H), 5.24 (d, J = 10.3 Hz, 1H), 4.43 (dd, J = 13.8, 6.7 Hz, 2H), 4.12 (dd, J = 15.8, 5.4 Hz, 1H), 3.20 (s, 3H), 1.43 (d, J = 6.8 Hz, 3H). MS [M+H]: *m/z* 362.2. **Yield** = 51% (21mg).

(*R*)-2-(3,5-Difluoro-4-hydroxy-phenylamino)-5,7-dimethyl-8-prop-2-ynyl-7,8-dihydro-5*H*-pteridin-6-one (11) beige solid. ^{1}H NMR (400MHz, DMSO-d6): δ 10.37 (bs, 1H), 9.92 (bs, 1H), 7.83 (s, 1H), 7.40-7.39 (d, *J* = 9.6Hz, 2H), 4.59-4.55 (q, *J* = 6.76Hz, 1H), 4.51-4.40 (qd, *J* = 2.32Hz/17.6Hz, 2H), 3.41-3.40 (t, *J* = 2.36Hz, 1H), 3.20 (s, 3H), 1.50-1.49 (d, *J* = 6.76Hz, 3H). ^{13}C NMR (100MHz, DMSO-d6): δ 163.2, 153.1, 153.0, 151.2, 151.1, 115.3, 104.5, 104.4, 78.3, 75.5, 57.2, 56.0, 35.9, 28.2, 18.2. HRMS calc. [M+H 360.1267] HRMS observed [M+H 360.1270]. Yield = 55% (30mg).

***(R)*-8-Benzyl-2-(3,5-difluoro-4-hydroxy-phenylamino)-5,7-dimethyl-7,8-dihydro-5*H*-pteridin-6-one *(*12)** grey solid. ^{1}H NMR (400MHz, DMSO-d6): δ 10.25 (bs, 1H), 9.91 (bs, 1H), 7.81 (s, 1H), 7.34-7.30 (m, 5H), 7.16-7.15 (d, *J* = 8.96Hz, 2H), 5.13-5.10 (d, *J* = 15.56Hz, 1H), 4.68-4.65 (d, *J* = 15.56Hz, 1H), 4.39-4.35 (q, *J* = 6.44Hz, 1H), 3.22 (s, 3H), 1.39-1.38 (d, *J* = 6.76Hz, 3H). ^{13}C NMR (100MHz, DMSO-d6): δ 163.3, 152.9,

151.7, 151.0, 135.6, 128.6, 127.6, 127.4, 115.3, 104.9, 56.7, 48.7, 28.3, 18.2. MS [M+H]: *m/z* 412.2. Yield = 48% (55mg).

(*R*)-5-Butyl-2-(3,5-difluoro-4-hydroxy-phenylamino)-7,8-dimethyl-7,8-dihydro-*5H*-pteridin-6-one (13) light brown solid. ^{1}H NMR (400MHz, DMSO-d6): δ 10.30 (bs, 1H), 9.97 (bs, 1H), 7.79 (s, 1H), 7.33-7.31 (d, *J* = 9.6Hz, 2H), 4.45-4.41 (q, *J* = 6.8Hz, 1H), 3.84-3.74 (m, 2H), 3.15 (s, 3H), 1.52-1.46 (m, 2H), 1.41-1.39 (d, *J* = 6.8Hz, 3H), 1.35-1.27 (m, 2H), 0.92-0.89 (t, *J* = 7.23Hz, 3H). ^{13}C NMR (100MHz, DMSO-d6): δ 163.3, 153.1, 152.9, 151.8, 151.1, 151.0, 113.8, 104.8, 57.9, 33.6, 27.8, 19.3, 17.5, 13.7. MS [M+H]: *m/z* 378.1. Yield = 31% (8mg).

***(R)*-2-(3,5-Difluoro-4-hydroxy-phenylamino)-7,8-dimethyl-5-(3-methyl-butyl)-7,8-dihydro-5*H*-pteridin-6-one (14)** beige solid. ^{1}H NMR (400MHz, DMSO-d6): δ 10.39 (bs, 1H), 10.00 (bs, 1H), 7.72 (s, 1H), 7.31-7.29 (d, *J* = 9.61Hz, 2H), 4.46-4.42 (q, *J* = 6.87Hz, 1H), 3.81-3.78 (m, 2H), 3.14 (s, 3H), 1.64-1.58 (m, 1H), 1.41-1.37 (m, 4H), 0.94-0.93 (d, *J* = 2.29Hz, 3H), 0.92-0.91 (d, *J* = 2.14Hz, 3H). MS [M+H]: *m/z* 392.1. Yield = 32% (35mg).

(*R*)-2-((3,5-difluoro-4-hydroxyphenyl)-amino)-7,8-dimethyl-5-(3-methylbut-2-en-1-yl)-7,8-dihydropteridin-6(5H)-one (15) white solid. ^{1}H NMR (400MHz, DMSO-d6): δ 9.41 (bs, 1H), 9.16 (s, 1H), 7.67 (s, 1H), 7.48-7.45 (dd, J = 11Hz, 2H), 5.06-5.03 (t, J = 6.36Hz, 1H), 4.46 (s, 2H), 4.28-4.24 (q, J = 6.97Hz, 1H), 3.04 (s, 3H), 1.75 (s, 3H), 1.68 (s, 3H), 1.27-1.25 (d, J = 6.85Hz, 3H). MS [M+H]: *m/z* 390.2. Yield = 26% (15mg).

(*R*)-2-(3,5-Difluoro-4-hydroxy-phenylamino)-7,8-dimethyl-5-(5-methyl-isoxazol-3-ylmethyl)-7,8-dihydro-5H-pteridin-6-one (16) grey solid. ^{1}H NMR (400MHz, DMSO-d6): δ 9.47 (bs, 1H), 9.27 (bs, 1H), 7.74 (s, 1H), 7.45-7.43 (d, *J* = 10.38Hz, 2H), 6.11 (s, 1H), 5.16-5.13 (d, *J* = 16.2Hz, 1H), 5.05-5.02 (d, *J* = 16.35Hz, 1H), 4.38-4.34 (q, J = 6.6Hz, 1H), 3.07 (s, 3H), 2.36 (s, 3H), 1.32-1.31 (d, J = 6.76Hz, 3H). ^{13}C NMR (100MHz, DMSO-d6): δ 170.3, 164.1, 159.5, 153.1, 151.24, 151.2, 113.4, 101.8, 100.9, 57.8, 36.2, 32.5, 16.0, 11.8. HRMS calc. [M+H 417.1481] HRMS observed [M+H 417.1483]. Yield = 65% (41mg).

(*R*)-[2-(3,5-Difluoro-4-hydroxy-phenylamino)-7,8-dimethyl-6-oxo-7,8-dihydro-6*H*-pteridin-5-yl]-acetonitrile (17) beige solid. ^{1}H NMR (400MHz, DMSO-d6): δ 9.45 (bs, 1H), 9.29 (s, 1H), 7.97 (s, 1H), 7.48 – 7.46 (d, J = 11,0Hz, 2H), 5.11 – 5.08 (d, J = 17,76Hz, 1H), 5.02 – 4.99 (d, J = 17,76Hz, 1H), 4.41 – 4.37 (q, J = 6,76Hz, 1H), 3.06 (s, 3H), 1.31 – 1.29 (d, J = 6,76Hz, 3H). HRMS calc. [M+H 361.1219] HRMS observed [M+H 361.1234] Yield = 47% (7mg).

(*R*)-2-(3,5-Difluoro-4-hydroxy-phenylamino)-7-methyl-5-(5-methyl-isoxazol-3-ylmethyl)-8-prop-2-ynyl-7,8-dihydro-5H-pteridin-6-one (18) beige solid. ^{1}H NMR (400MHz, DMSO-d6): δ 9.43 (bs, 1H), 9.28 (bs, 1H), 7.84 (s, 1H), 7.49-7.47 (d, J = 10.69Hz, 2H), 6.12 (s, 1H), 5.18-5.14 (d, J = 16.35Hz, 1H), 5.06-5.02 (d, J = 16.19Hz, 1H), 4.54-4.47 (m, 2H), 4.31-4.27 (dd, J = 17.45/ 2.36Hz, 1H), 2.36 (s, 3H), 1.41-1.39 (d, J = 6.92Hz, 3H). HRMS calc. [M+H 441.1481] HRMS observed [M+H 441.1479]. Yield = 41% (9mg).

***(R)*-2-(2-((3,5-difluoro-4-hydroxyphenyl)amino)-7-methyl-6-oxo-8-(prop-2-yn-1-yl)-7,8-dihydropteridin-5(6H)-yl)acetonitrile (19)** beige solid. ^{1}H NMR (500 MHz, CD3OH) δ 7.91 (s, 1H), 7.35 (d, J = 10.5 Hz, 2H), 5.03 – 4.97 (m, 2H), 4.63 (dd, J = 17.6, 2.5 Hz, 1H), 4.58 – 4.55 (m, 1H), 4.30 (dd, J = 17.7, 2.4 Hz, 1H), 2.79 (t, J = 2.4 Hz, 1H), 1.52 (d, J = 6.9 Hz, 3H). ^{13}C NMR (126 MHz, CD3OH) δ 165.92, 157.41, 154.77, 154.70, 152.80, 152.23, 139.66, 133.60, 115.79, 114.12, 104.00, 103.93, 103.85, 103.78, 79.30, 74.52, 57.89, 35.64, 29.85, 16.94. MS [M+H]: m/z 385.2. Yield = 45% (14mg).

(*R*)-2-(3,5-Difluoro-4-hydroxy-phenylamino)-5-ethyl-7-methyl-8-prop-2-ynyl-7,8-dihydro-5*H*-pteridin-6-one (20) beige solid. ^{1}H NMR (400MHz, DMSO-d6): δ 9.41 (bs, 1H), 9.26 (bs, 1H), 7.95 (s, 1H), 7.51-7.49 (d, *J* = 10.7Hz, 2H), 4.54-4.50 (dd, *J* = 2.20Hz/ 17.45Hz, 1H), 4.40-4.36 (q, *J* = 6.76Hz, 1H), 4.28-2.24 (dd, *J* = 2.36Hz/ 17.61Hz, 1H), 3.89-3.84 (m, 2H), 3.30-3.29 (t, *J* = 2.36Hz, 1H), 1.35-1.34 (d, *J* = 6.76Hz, 3H), 1.12-1.09 (t, *J* = 7.07Hz, 3H). ^{13}C NMR (100MHz, DMSO-d6): δ 163.2, 154.9, 153.2, 153.1, 151.3, 151.2, 150.4, 138.9, 132.9, 126.8, 126.6, 113.2, 101.8, 101.6, 79.4, 75.0, 56.3, 35.4, 34.3, 16.5, 11.9. MS [M+H]: *m/z* 374.2. Yield = 45% (20mg).

(*R*)-2-(3,5-Difluoro-4-hydroxy-phenylamino)-5-isoxazol-5-ylmethyl-7-methyl-8-prop-2-ynyl-7,8-dihydro-5H-pteridin-6-one (21) beige solid. ^{1}H NMR (400MHz, DMSO-d6): δ 9.43 (bs, 1H), 9.29 (bs, 1H), 8.52 (s, 1H), 7.94 (s, 1H), 7.49-7.47 (d, *J* = 10.69Hz, 2H), 6.47 (s, 1H), 5.34-5.31 (d, *J* = 16.82Hz, 1H), 5.27-5.23 (d, *J* = 16.82Hz, 1H), 4.53-4.48 (m, 2H), 4.32-4.28 (dd, *J* = 17.45/ 2.20Hz, 1H), 1.41-1.40 (d, *J* = 6.76Hz, 3H). HRMS calc. [M+H 427.1325] HRMS observed [M+H 427.1323]. Yield = 38% (8mg).

***(R)*-2-[(3,5-difluoro-4-hydroxyphenyl)-amino]-5-(3-hydroxy-3-methylbutyl)-7-methyl-8-(prop-2-yn-1-yl)-5,6,7,8-tetrahydropteridin-6-one (22)** white solid. ^{1}H NMR (400MHz, DMSO-d6): δ 10.14 (bs, 1H), 9.96 (bs, 1H), 7.64 (s, 1H), 7.33-7.31 (d, *J* = 7.86Hz, 2H), 4.41 (m, 1H), 3.89-3.82 (m, 3H), 3.13 (s, 3H), 1.61-1.58 (t, *J* = 7.86Hz, 2H), 1.39-1.37 (d, *J* = 5.87Hz, 3H), 1.16 (s, 6H). MS [M+H]: *m/z* 432.2. Yield = 6% (5mg).

(*R*)-2-((3-amino-1H-indazol-6-yl)amino)-7-methyl-5,8-di(prop-2-yn-1-yl)-7,8-dihydropteridin-6(5H)-one (23) white solid. ^{1}H NMR (400MHz, DMSO-d6): δ 11.05 (s, 1H), 9.28 (s, 1H), 7.99 (s, 1H), 7.94 (s, 1H), 7.49 (d, *J*=8.5 Hz, 1H), 7.13 (dd, *J*=1.4, 8.7 Hz, 1H), 5.15 (s, 2H), 4.79 - 4.65 (m, 3H), 4.46 (q, *J*=6.9 Hz, 1H), 4.25

(dd, *J*=2.5, 17.6 Hz, 1H), 3.38 - 3.35 (m, 1H), 3.31 - 3.25 (m, 1H), 1.38 (d, *J*=6.8 Hz, 3H). MS [M+H]: *m/z* 387.1. Yield = 11% (15mg).

(*R*)-2-((3-hydroxy-1H-indazol-6-yl)-amino)-7-methyl-5,8-di(prop-2-yn-1-yl)-7,8-dihydropteridin-6(5H)-one (24) white solid. ^{1}H NMR (400MHz, DMSO-d_6) δ 10.69 (br, 1H), 9.51 (s, 1H), 8.03 - 7.97 (m, 2H), 7.44 (d, *J*=8.5 Hz, 1H), 7.20 (dd, *J*=1.5, 8.8 Hz, 1H), 4.74 (s, 2H), 4.66 (dd, *J*=2.5, 17.6 Hz, 1H), 4.48 (q, *J*=6.8 Hz, 1H), 4.28 (dd, *J*=2.3, 17.6 Hz, 1H), 3.33 - 3.24 (m, 2H), 1.39 (d, *J*=6.8 Hz, 3H). HRMS calc. [M+H 388.1516] HRMS observed [M+H 388.1519]. Yield = 25% (11mg).

(*R*)-2-((2-amino-4-methylbenzo[d]thiazol-6-yl)-amino)-7-methyl-5,8-di(prop-2-yn-1-yl)-7,8-dihydropteridin-6(5H)-one (25) light beige solid. ^{1}H NMR (400MHz, DMSO-d_6) δ 9.47 (br s, 1H), 8.04 (br s, 1H), 7.88 (s, 1H), 7.57 (br s, 2H), 7.33 (s, 1H), 4.71 (s, 2H), 4.54 - 4.47 (m, 2H), 4.33 (br d, *J*=19.3 Hz, 1H), 3.38 (s, 1H), 3.33 (s, 1H), 2.40 (s, 3H), 1.41 (d, *J*=6.8 Hz, 3H). MS [M+H]: *m/z* 418.2. Yield = 22% (14mg).

(*R*)-(3-fluoro-4-((7-methyl-6-oxo-5,8-di(prop-2-yn-1-yl)-5,6,7,8-tetrahydropteridin-2-yl)-amino)-phenyl)-boronic acid (26) Off-white solid. ^{1}H NMR (400MHz, DMSO-d_6) δ 8.75 (br s, 1H), 8.16 - 8.00 (m, 2H), 7.94 (s, 1H), 7.60 - 7.37 (m, 2H), 4.71 (s, 2H), 4.57 (dd, *J*=2.4, 17.7 Hz, 1H), 4.47 (d, *J*=7.0 Hz, 1H), 4.23 (dd, *J*=2.3, 17.8 Hz, 1H), 3.32 - 3.17 (m, 2H), 1.38 (d, *J*=6.8 Hz, 3H). MS [M+H]: *m/z* 394.0. Yield = 32% (14mg).

(*R*)-(4-((7-methyl-6-oxo-5,8-di(prop-2-yn-1-yl)-5,6,7,8-tetrahydropteridin-2-yl)amino)phenyl)boronic acid (27) white solid. ^{1}H NMR (400MHz, DMSO-d_6) δ 9.56 (br s, 1H), 7.96 (s, 1H), 7.77 - 7.69 (m, 4H), 4.77 - 4.68 (m, 2H), 4.58 (dd, *J*=2.3, 17.6 Hz, 1H), 4.50 (q, *J*=6.8 Hz, 1H), 4.32 (br d, *J*=17.6 Hz, 1H), 3.50 - 3.24 (m, 2H), 1.41 (d, *J*=6.8 Hz, 3H). MS [M+H]: *m/z* 376.0. Yield = 30% (25mg).

(*R*)-2-((3-chloro-4-hydroxyphenyl)amino)-7-methyl-5,8-di-(prop-2-yn-1-yl)-7,8-dihydropteridin-6(5H)-one (28) Off-white solid. ^{1}H NMR (400MHz, DMSO-d_6) δ 9.62 (s, 1H), 9.19 (br s, 1H), 7.93 (s, 1H), 7.86 (d, *J*=2.4 Hz, 1H), 7.44 (dd, *J*=2.6, 8.8 Hz, 1H), 6.86 (d, *J*=8.8 Hz, 1H), 4.78 - 4.63 (m, 2H), 4.56 (dd, *J*=2.3, 17.5 Hz, 1H), 4.45 (q, *J*=6.7 Hz, 1H), 4.25 (dd, *J*=2.3, 17.6 Hz, 1H), 3.35 - 3.28 (m, 2H), 1.37 (d, *J*=6.8 Hz, 3H). MS [M+H]: *m/z* 381.9. Yield = 33% (18.5mg).

(*R*)-2-(benzo[d]isoxazol-5-ylamino)-7-methyl-5,8-di(prop-2-yn-1-yl)-7,8-dihydropteridin-6(5H)-one (29) Light beige solid. ^{1}H NMR (400MHz, DMSO-d_6) δ 9.56 (s, 1H), 9.13 (d, *J*=1.0 Hz, 1H), 8.48 (d, *J*=2.0 Hz, 1H), 7.99 (s, 1H), 7.85 (dd, *J*=2.2, 9.0 Hz, 1H), 7.67 (d, *J*=9.0 Hz, 1H), 4.73 (s, 2H), 4.60 - 4.46 (m, 2H), 4.31 (dd, *J*=2.3, 17.5 Hz, 1H), 3.40 (t, *J*=2.4 Hz, 1H), 3.32 (t, *J*=2.4 Hz, 1H), 1.39 (d, *J*=6.8 Hz, 3H). MS [M+H]: *m/z* 373.3. Yield = 34% (20mg).

(*R*)-2-((3-bromo-1H-indazol-6-yl)amino)-7-methyl-5,8-di(prop-2-yn-1-yl)-7,8-dihydropteridin-6(5H)-one (30) Beige solid. ^{1}H NMR (400MHz, DMSO-d_6) δ 13.22 (s, 1H), 9.45 (s, 1H), 8.25 (s, 1H), 8.01 (s, 1H), 7.64 (dd, *J*=1.9, 9.2 Hz, 1H), 7.46 (d, *J*=9.0 Hz, 1H), 4.75 - 4.66 (m, 3H), 4.49 - 4.43 (m, 1H), 4.32 (d, *J*=2.5 Hz, 1H), 4.28 (d, *J*=2.3 Hz, 1H), 3.32 - 3.26 (m, 2H), 1.38 (d, *J*=6.8 Hz, 3H). MS [M+H]: *m/z* 450.1/452.1. Yield = 35% (19mg).

Methyl (*R*)-2-hydroxy-5-((7-methyl-6-oxo-5,8-di(prop-2-yn-1-yl)-5,6,7,8-tetrahydropteridin-2-yl)amino) benzoate (31) white solid. ^{1}H NMR (400MHz, DMSO-d6): δ 10.17 (bs, 1H), 9.29 (bs, 1H), 8.46-8.45 (d, J = 2.7Hz, 1H), 7.96 (s, 1H), 7.77-7.74 (dd, J = 2.69/ 8.8Hz, 1H), 6.92-6.90 (d, J = 8.93Hz, 1H), 4.72 (s, 2H), 4.47-4.42 (q, J = 6.72Hz, 1H), 4.28-4.23 (dd, J = 2.20/ 17.61Hz, 1H), 3.91 (s, 3H), 3.32 – 3.30 (m, 1H), 1.37-1.35 (d, J = 6.85Hz, 3H). MS [M+H]: *m/z* 406.2. Yield = 54% (32mg).

(*R*)-2-Fluoro-4-(7-methyl-6-oxo-5,8-di-prop-2-ynyl-5,6,7,8-tetrahydro-pteridin-2-ylamino)-benzoic acid (32) White solid. ^{1}H NMR (400MHz, DMSO-d6): δ 10.48 (s, 1H), 8.02 (s, 1H), 7.91-7.87 (dd, *J* = 2Hz/ 14Hz, 1H), 7.83-7.78 (t, *J* = 8.7Hz, 1H), 7.54-7.51 (dd, *J* = 2Hz/ 8.7Hz, 1H), 4.72 (s, 2H), 4.61-4.56 (q, *J* = 6.85Hz, 1H), 4.54-4.49 (dd, *J* = 2.4Hz/17.6Hz, 1H), 4.44-4.39 (dd, *J* = 2.4Hz/ 17.6Hz, 1H), 3.41-3.40 (t, *J* = 2.32Hz, 1H), 3.36-3.35 (t, *J* = 2.32Hz, 1H), 1.46-1.45 (d, *J* = 6.85Hz, 3H). ^{13}C NMR (100MHz, DMSO-d6): δ 164.7, 163.1, 160.8, 152.2, 150.7, 145.3, 132.5, 114.1, 113.7, 111.4, 105.9, 105.6, 78.8, 77.6, 75.4, 56.9, 35.5, 30.3, 17.4. MS [M+H]: *m/z* 394.4. Yield = 43% (70mg).

(*R*)-7-methyl-2-((1-oxo-1,2-dihydroisoquinolin-6-yl)-amino)-5,8-di-(prop-2-yn-1-yl)-7,8-dihydropteridin-6(5H)-one (33) Off-white solid. ^{1}H NMR (400MHz, DMSO-d_6) δ 10.95 (br d, *J*=5.0 Hz, 1H), 9.79 (s, 1H), 8.31 (s, 1H), 8.05 - 8.00 (m, 2H), 7.65 (br d, *J*=8.5 Hz, 1H), 7.09 (t, *J*=6.4 Hz, 1H), 6.43 (d, *J*=7.3 Hz, 1H), 4.74 (br s, 2H), 4.54 - 4.48 (m, 2H), 4.42 - 4.35 (m, 1H), 3.39 (s, 1H), 3.32 (s, 1H), 1.40 (d, *J*=6.5 Hz, 3H). MS [M+H]: *m/z* 399.3. Yield = 40% (24mg).

(*R*)-7-methyl-2-((1-oxoisoindolin-5-yl)-amino)-5,8-di(prop-2-yn-1-yl)-7,8-dihydropteridin-6(5H)-one (34) Off-white solid. ^{1}H NMR (400MHz, DMSO-d_6) δ 9.75 (s, 1H), 8.26 (d, *J*=5.5 Hz, 2H), 8.00 (s, 1H), 7.69 (dd, *J*=1.8, 8.3 Hz, 1H), 7.52 (d, *J*=8.3 Hz, 1H), 4.73 (s, 2H), 4.55 - 4.47 (m, 2H), 4.36 - 4.29 (m, 3H), 3.39 (t, *J*=2.4 Hz, 1H), 3.32 (t, *J*=2.4 Hz, 1H), 1.39 (d, *J*=6.8 Hz, 3H). MS [M+H]: *m/z* 387.2. Yield = 31% (18mg).

***(S)*-2-((3,5-difluoro-4-hydroxyphenyl)amino)-7,8-dimethyl-5-(prop-2-yn-1-yl)-7,8-dihydropteridin-6(5H)-one (35)** white solid. ^{1}H NMR (400 MHz, DMSO-d6) δ 9.44 (s, 1H), 9.22 (s, 1H), 7.86 (s, 1H), 7.47 (d, J = 11.2 Hz, 2H), 4.69 (dd, J = 4.1, 2.5 Hz, 2H), 4.32 (q, J = 6.8 Hz, 1H), 3.27 (t, J = 2.3 Hz, 1H), 3.05 (s, 3H), 1.27 (d, J = 6.8 Hz, 3H).^{13}C NMR (126 MHz, CD3OH) δ 165.67, 153.26, 138.00, 114.36, 104.20, 78.16, 74.27,

59.95, 33.38, 31.28, 16.52. HRMS calc. [M+H 392.1267] HRMS observed [M+H 392.1274]. Yield = 38% (21mg).

***(S)-2-((3,5-difluoro-4-hydroxyphenyl)amino)-7,8-dimethyl-5-((3-methylisoxazol-5-yl)methyl)-7,8-dihydropteridin-6(5H)-one* (36)** beige solid. ^{1}H NMR (500 MHz, CD3OH) δ 7.83 (s, 1H), 7.33 (d, J = 10.6 Hz, 2H), 6.26 (s, 1H), 5.34 (d, J = 16.8 Hz, 1H), 5.15 (d, J = 16.7 Hz, 1H), 4.66 (dd, J = 17.7, 2.4 Hz, 1H), 4.57 (dd, J = 13.7, 6.8 Hz, 1H), 4.29 (dd, J = 17.7, 2.4 Hz, 1H), 2.79 (t, J = 2.4 Hz, 1H), 2.26 (s, 2H), 1.51 (d, J = 6.9 Hz, 3H). MS [M+H]: m/z 441.2. Yield = 34% (12.5mg).

***(S)-2-(2-((3,5-difluoro-4-hydroxyphenyl)amino)-7,8-dimethyl-6-oxo-7,8-dihydropteridin-5(6H)-yl)acetonitrile* (37)** off-white solid. ^{1}H NMR (500 MHz, CD3OH) δ 7.82 (s, 1H), 7.31 (d, J = 10.1 Hz, 2H), 5.00 (d, J = 6.0 Hz, 2H), 4.36 (dt, J = 12.7, 6.3 Hz, 1H), 3.16 (s, 3H), 1.43 (d, J = 6.9 Hz, 3H). ^{13}C NMR (126 MHz, CD3OH) δ 166.02, 157.51, 153.10, 138.29, 115.79, 114.03, 104.03, 59.84, 33.38, 29.69, 16.49. MS [M+H]: m/z 361.1. Yield = 43% (16mg).

***(S)*-2-((3,5-difluoro-4-hydroxyphenyl)amino)-7-methyl-5-((3-methylisoxazol-5-yl)methyl)-8-(prop-2-yn-1-yl)-7,8-dihydropteridin-6(5H)-one (38)** beige solid. ^{1}H NMR (500 MHz, CD3OH) δ 7.83 (s, 1H), 7.33 (d, J = 10.6 Hz, 2H), 6.26 (s, 1H), 5.34 (d, J = 16.8 Hz, 1H), 5.15 (d, J = 16.7 Hz, 1H), 4.66 (dd, J = 17.7, 2.4 Hz, 1H), 4.57 (dd, J = 13.7, 6.8 Hz, 1H), 4.29 (dd, J = 17.7, 2.4 Hz, 1H), 2.79 (t, J = 2.4 Hz, 1H), 2.26 (s, 2H), 1.51 (d, J = 6.9 Hz, 3H). MS [M+H]: m/z 441.2. Yield = 34% (12.5mg).

***(S)-2-(2-((3,5-difluoro-4-hydroxyphenyl)amino)-7-methyl-6-oxo-8-(prop-2-yn-1-yl)-7,8-dihydropteridin-5(6H)-yl)acetonitrile* (39)** beige solid. ^{1}H NMR (500 MHz, CD3OH) δ 7.92 (s, 1H), 7.35 (d, J = 10.6 Hz, 2H), 5.01 (d, J = 13.2 Hz, 2H), 4.65 (dd, J = 17.7, 2.5 Hz, 1H), 4.59 – 4.55 (m, 1H), 4.30 (dd, J = 17.7, 2.4 Hz, 1H), 2.17 (s, 1H), 1.52 (d, J = 6.9 Hz, 3H). ^{13}C NMR (126 MHz, CD3OH) δ 165.94, 157.50, 152.24, 139.82, 115.79, 114.12, 103.99, 103.77, 79.31, 74.51, 57.88, 35.61, 29.84, 16.91. MS [M+H]: m/z 385.2. Yield = 37% (15mg).

(*S*)-2-((3-hydroxy-1H-indazol-6-yl)amino)-7-methyl-5,8-di(prop-2-yn-1-yl)-7,8-dihydropteridin-6(5H)-one (40) Off white solid. ^{1}H NMR (500 MHz, DMSO) δ 10.61 (s, 1H), 9.45 (s, 1H), 8.02 – 7.99 (m, 2H), 7.43 (d, J = 8.6 Hz, 1H), 7.20 (dd, J = 8.7, 1.7 Hz, 1H), 4.73 (s, 2H), 4.66 (dd, J = 17.6, 2.5 Hz, 1H), 4.47 (q, J = 6.8 Hz, 1H), 4.26 (dd, J = 17.6, 2.4 Hz, 1H), 3.35 (t, J = 2.4 Hz, 1H), 3.30 (d, J = 2.4 Hz, 1H), 1.37 (d, J = 6.8 Hz, 3H). ^{13}C NMR (126 MHz, DMSO) δ 163.3, 155.5, 150.3, 141.5, 139.6, 120.7, 112.8, 112.7, 108.2, 97.8, 79.3, 78.2, 75.3, 75.0, 56.0, 45.6, 34.1, 30.0, 21.2, 16.3. MS [M+H]: m/z 388.3. Yield = 39% (14mg).

***(S)*-2-((3,5-difluoro-4-hydroxyphenyl)-amino)-7-methyl-5,8-di(prop-2-yn-1-yl)-7,8-dihydropteridin-6(5H)-one (41)** white solid. ^{1}H NMR (500 MHz, CD3OH) δ 7.94 (s, 1H), 7.35 (d, J = 10.5 Hz, 1H), 4.82 (dd, J = 17.8, 2.4 Hz, 1H), 4.65 (dd, J = 17.5, 2.3 Hz, 1H), 4.52 (q, J = 6.8 Hz, 1H), 4.28 (dd, J = 17.7, 2.4 Hz, 1H), 2.78 (dd, J = 4.4, 2.3 Hz, 1H), 1.49 (d, J = 6.9 Hz, 1H). ^{13}C NMR (126 MHz, CD3OH) δ 165.65, 157.28, 152.27, 140.50, 114.38, 103.85, 103.64, 79.42, 78.22, 74.41, 74.25, 57.90, 35.46, 31.38, 16.82. MS [M+H]: m/z 384.2. Yield = 42% (17mg).

***(R)*-2-((3,5-difluoro-4-hydroxyphenyl)amino)-4,7,8-trimethyl-5-(prop-2-yn-1-yl)-7,8-dihydropteridin-6(5H)-one (42)** beige solid. ^{1}H NMR (500 MHz, DMSO) δ 10.05 (bs, 2H), 7.32 (d, *J* = 9.5 Hz, 2H), 4.58 (dd, *J* = 18.1, 2.3 Hz, 1H), 4.47 (dd, *J* = 18.1, 2.4 Hz, 1H), 4.38 (q, *J* = 6.8 Hz, 1H), 3.39 (s, 1H), 3.14 (s, 3H), 2.57 (s, 3H), 1.26 (d, *J* = 6.9 Hz, 3H). ^{13}C NMR (126 MHz, DMSO) δ 166.0, 154.4, 153.1, 153.0, 151.2, 151.1, 112.6, 104.4, 79.2, 75.7, 58.5, 36.2, 33.6, 14.7. MS [M+H]: *m/z* 374.1. Yield = 29% (10mg).

Acknowledgments

We thank all members of CQMED-UNICAMP for their help and support. We thank the staff of the Life Sciences Core Facility (LaCTAD) at UNICAMP for the Genomics and Mass Spectrometry analysis. We thank the NMR facility at UNICAMP Chemistry Institute for its assistance. We thank the staff at the Northeastern Collaborative Access Team beamlines, which are funded by the National Institute of General Medical Sciences from the National Institutes of Health (P41 GM103403). The Pilatus 6M detector on the 24-ID-C beamline is funded by a NIH-ORIP HEI grant (S10 RR029205). This research used resources of the Advanced Photon Source; a U.S. Department of Energy (DOE) Office of Science User Facility operated for the DOE Office of Science by Argonne National Laboratory under Contract No. DE-AC02-06CH11357. We thank Diamond Light Source for access to beam line I24. The authors thank Tammy Havener (SGC-UNC), Abid Hussain Sayyid (KI), Bruno Urien (KI) and Ann-Sofie Nillson (KI) for valuable discussions and technical support.

Funding

R.M.C. and K.B.M. are grateful for support by FAPESP (Fundação de Amparo à Pesquisa do Estado de São Paulo) (grants 2013/50724-5 and 2014/50897-0), Embrapii (Empresa Brasileira de Pesquisa e Inovação Industrial), CNPq (Conselho Nacional de Desenvolvimento Científico e Tecnológico) (grant 465651/2014-3) and Aché Laboratórios Farmacêuticos. R.M.C. and O.G. are also grateful for support by the Structural Genomics Consortium, a registered charity (1097737) that receives funds from AbbVie, Bayer AG, Boehringer Ingelheim, Canada Foundation for Innovation, Eshelman Institute for Innovation, Genentech, Genome Canada through the Ontario Genomics Institute (OGI-196), EU/EFPIA/OICR/McGill/KTH/Diamond, Innovative Medicines Initiative 2 Joint Undertaking (EUbOPEN Grant 875510), Janssen, Merck KGaA, Merck & Co., Pfizer, Takeda, and Wellcome. B.L. and M.H. are grateful for support from the Swedish Research Council, Swedish Cancer Society, Karolinska Institutet and The Mark Foundation for Cancer Research. R.A.M.S. (2016/25320-6 and 2018/23322-7), A.S.S. (2019/14275-8), S.N.S.V (2018/09475-5), V.M.A. (2022/00743-2) and M.R.C. (2021/04853-4) were recipients of fellowships from the Fundação de Amparo à Pesquisa do Estado de São Paulo, FAPESP. C.V.R. (88887.146077/2017-00), J.E.T. (88887.373547/2019-00) and P.Z.R (88887.136432/2017-00) were the recipient of fellowships from the Coordenação de Aperfeiçoamento de Pessoal de Nível Superior, CAPES.

References

(1) Banham, A. H.; Smith, G. L. Vaccinia Virus Gene B1R Encodes a 34-kDa Serine/Threonine Protein Kinase That Localizes in Cytoplasmic Factories and Is Packaged into Virions. *Virology* **1992**, *191* (2), 803–812. https://doi.org/10.1016/0042-6822(92)90256-O.

(2) Boyle, K. A.; Traktman, P. Members of a Novel Family of Mammalian Protein Kinases Complement the DNA-Negative Phenotype of a Vaccinia Virus *Ts* Mutant Defective in the B1 Kinase. *J. Virol.* **2004**, *78* (4), 1992–2005. https://doi.org/10.1128/JVI.78.4.1992-2005.2004.

(3) Scheeff, E. D.; Eswaran, J.; Bunkoczi, G.; Knapp, S.; Manning, G. Structure of the Pseudokinase VRK3 Reveals a Degraded Catalytic Site, a Highly Conserved Kinase Fold, and a Putative Regulatory Binding Site. *Structure* **2009**, *17* (1), 128–138. https://doi.org/10.1016/j.str.2008.10.018.

(4) Ben, Z.; Gong, L.; Qiu, Y. High Expression of VRK1 Is Related to Poor Prognosis in Glioma. *Pathol. - Res. Pract.* **2018**, *214* (1), 112–118. https://doi.org/10.1016/j.prp.2017.10.014.

(5) Colmenero-Repiso, A.; Gómez-Muñoz, M. A.; Rodríguez-Prieto, I.; Amador-Álvarez, A.; Henrich, K.-O.; Pascual-Vaca, D.; Okonechnikov, K.; Rivas, E.; Westermann, F.; Pardal, R.; Vega, F. M. Identification of VRK1 as a New Neuroblastoma Tumor Progression Marker Regulating Cell Proliferation. *Cancers* **2020**, *12* (11), 3465. https://doi.org/10.3390/cancers12113465.

(6) Fournier, M. V.; Martin, K. J.; Kenny, P. A.; Xhaja, K.; Bosch, I.; Yaswen, P.; Bissell, M. J. Gene Expression Signature in Organized and Growth-Arrested Mammary Acini Predicts Good Outcome in Breast Cancer. *Cancer Res.* **2006**, *66* (14), 7095–7102. https://doi.org/10.1158/0008-5472.CAN-06-0515.

(7) Hennig, E. E.; Mikula, M.; Rubel, T.; Dadlez, M.; Ostrowski, J. Comparative Kinome Analysis to Identify Putative Colon Tumor Biomarkers. *J. Mol. Med.* **2012**, *90* (4), 447–456. https://doi.org/10.1007/s00109-011-0831-6.

(8) Kim, I.-J.; Quigley, D.; To, M. D.; Pham, P.; Lin, K.; Jo, B.; Jen, K.-Y.; Raz, D.; Kim, J.; Mao, J.-H.; Jablons, D.; Balmain, A. Rewiring of Human Lung Cell Lineage and Mitotic Networks in Lung Adenocarcinomas. *Nat. Commun.* **2013**, *4* (1), 1701. https://doi.org/10.1038/ncomms2660.

(9) Martin, K. J.; Patrick, D. R.; Bissell, M. J.; Fournier, M. V. Prognostic Breast Cancer Signature Identified from 3D Culture Model Accurately Predicts Clinical Outcome across Independent Datasets. *PLoS ONE* **2008**, *3* (8), e2994. https://doi.org/10.1371/journal.pone.0002994.

(10) Mon, A. M.; MacKinnon, A. C.; Traktman, P. Overexpression of the VRK1 Kinase, Which Is Associated with Breast Cancer, Induces a Mesenchymal to Epithelial Transition in Mammary Epithelial Cells. *PLOS ONE* **2018**, *13* (9), e0203397. https://doi.org/10.1371/journal.pone.0203397.

(11) Riggi, N.; Knoechel, B.; Gillespie, S. M.; Rheinbay, E.; Boulay, G.; Suvà, M. L.; Rossetti, N. E.; Boonseng, W. E.; Oksuz, O.; Cook, E. B.; Formey, A.; Patel, A.; Gymrek, M.; Thapar, V.; Deshpande, V.; Ting, D. T.; Hornicek, F. J.; Nielsen, G. P.; Stamenkovic, I.; Aryee, M. J.; Bernstein, B. E.; Rivera, M. N. EWS-FLI1 Utilizes Divergent Chromatin Remodeling Mechanisms to Directly Activate or Repress Enhancer Elements in Ewing Sarcoma. *Cancer Cell* **2014**, *26* (5), 668–681. https://doi.org/10.1016/j.ccell.2014.10.004.

(12) Valbuena, A.; Suárez-Gauthier, A.; López-Rios, F.; López-Encuentra, A.; Blanco, S.; Fernández, P. L.; Sánchez-Céspedes, M.; Lazo, P. A. Alteration of the VRK1-P53 Autoregulatory Loop in Human Lung Carcinomas. *Lung Cancer* **2007**, *58* (3), 303–309. https://doi.org/10.1016/j.lungcan.2007.06.023.

(13) Li, J.; Wang, T.; Pei, L.; Jing, J.; Hu, W.; Sun, T.; Liu, H. Expression of VRK1 and the Downstream Gene BANF1 in Esophageal Cancer. *Biomed. Pharmacother.* **2017**, *89*, 1086–1091. https://doi.org/10.1016/j.biopha.2017.02.095.

(14) Campillo-Marcos, I.; Lazo, P. A. Olaparib and Ionizing Radiation Trigger a Cooperative DNA-Damage Repair Response That Is Impaired by Depletion of the VRK1 Chromatin Kinase. *J. Exp. Clin. Cancer Res.* **2019**, *38* (1), 203. https://doi.org/10.1186/s13046-019-1204-1.

(15) Molitor, T. P.; Traktman, P. Molecular Genetic Analysis of VRK1 in Mammary Epithelial Cells: Depletion Slows Proliferation in Vitro and Tumor Growth and Metastasis in Vivo. *Oncogenesis* **2013**, *2* (6), e48–e48. https://doi.org/10.1038/oncsis.2013.11.
(16) Navarro-Carrasco, E.; Lazo, P. A. VRK1 Depletion Facilitates the Synthetic Lethality of Temozolomide and Olaparib in Glioblastoma Cells. *Front. Cell Dev. Biol.* **2021**, *9*, 683038. https://doi.org/10.3389/fcell.2021.683038.
(17) Shields, J. A.; Meier, S. R.; Bandi, M.; Mulkearns-Hubert, E. E.; Hajdari, N.; Ferdinez, M. D.; Engel, J. L.; Silver, D. J.; Shen, B.; Zhang, W.; Hubert, C. G.; Mitchell, K.; Shakya, S.; Zhao, S.-C.; Bejnood, A.; Zhang, M.; Tjin Tham Sjin, R.; Wilker, E.; Lathia, J. D.; Andersen, J. N.; Chen, Y.; Li, F.; Weber, B.; Huang, A.; Emmanuel, N. VRK1 Is a Synthetic–Lethal Target in VRK2-Deficient Glioblastoma. *Cancer Res.* **2022**, *82* (21), 4044–4057. https://doi.org/10.1158/0008-5472.CAN-21-4443.
(18) So, J.; Mabe, N. W.; Englinger, B.; Chow, K.-H.; Moyer, S. M.; Yerrum, S.; Trissal, M. C.; Marques, J. G.; Kwon, J. J.; Shim, B.; Pal, S.; Panditharatna, E.; Quinn, T.; Schaefer, D. A.; Jeong, D.; Mayhew, D. L.; Hwang, J.; Beroukhim, R.; Ligon, K. L.; Stegmaier, K.; Filbin, M. G.; Hahn, W. C. VRK1 as a Synthetic Lethal Target in VRK2 Promoter–Methylated Cancers of the Nervous System. *JCI Insight* **2022**, *7* (19), e158755. https://doi.org/10.1172/jci.insight.158755.
(19) Nichols, R. J.; Wiebe, M. S.; Traktman, P. The Vaccinia-Related Kinases Phosphorylate the N' Terminus of BAF, Regulating Its Interaction with DNA and Its Retention in the Nucleus. *Mol. Biol. Cell* **2006**, *17* (5), 2451–2464. https://doi.org/10.1091/mbc.e05-12-1179.
(20) Haraguchi, T.; Koujin, T.; Segura-Totten, M.; Lee, K. K.; Matsuoka, Y.; Yoneda, Y.; Wilson, K. L.; Hiraoka, Y. BAF Is Required for Emerin Assembly into the Reforming Nuclear Envelope. *J. Cell Sci.* **2001**, *114* (24), 4575–4585. https://doi.org/10.1242/jcs.114.24.4575.
(21) Samwer, M.; Schneider, M. W. G.; Hoefler, R.; Schmalhorst, P. S.; Jude, J. G.; Zuber, J.; Gerlich, D. W. DNA Cross-Bridging Shapes a Single Nucleus from a Set of Mitotic Chromosomes. *Cell* **2017**, *170* (5), 956-972.e23. https://doi.org/10.1016/j.cell.2017.07.038.
(22) Campillo-Marcos, I.; García-González, R.; Navarro-Carrasco, E.; Lazo, P. A. The Human VRK1 Chromatin Kinase in Cancer Biology. *Cancer Lett.* **2021**, *503*, 117–128. https://doi.org/10.1016/j.canlet.2020.12.032.
(23) Lopez-Borges, S.; Lazo, P. A. The Human Vaccinia-Related Kinase 1 (VRK1) Phosphorylates Threonine-18 within the Mdm-2 Binding Site of the P53 Tumour Suppressor Protein. *Oncogene* **2000**, *19* (32), 3656–3664. https://doi.org/10.1038/sj.onc.1203709.
(24) Molitor, T. P.; Traktman, P. Depletion of the Protein Kinase VRK1 Disrupts Nuclear Envelope Morphology and Leads to BAF Retention on Mitotic Chromosomes. *Mol. Biol. Cell* **2014**, *25* (6), 891–903. https://doi.org/10.1091/mbc.e13-10-0603.
(25) Salzano, M.; Sanz-García, M.; Monsalve, D. M.; Moura, D. S.; Lazo, P. A. VRK1 Chromatin Kinase Phosphorylates H2AX and Is Required for Foci Formation Induced by DNA Damage. *Epigenetics* **2015**, *10* (5), 373–383. https://doi.org/10.1080/15592294.2015.1028708.
(26) Blanco, S.; Klimcakova, L.; Vega, F. M.; Lazo, P. A. The Subcellular Localization of Vaccinia-Related Kinase-2 (VRK2) Isoforms Determines Their Different Effect on P53 Stability in Tumour Cell Lines: Differential Stabilization of P53 by VRK2 Isoforms. *FEBS J.* **2006**, *273* (11), 2487–2504. https://doi.org/10.1111/j.1742-4658.2006.05256.x.
(27) Birendra, K.; May, D. G.; Benson, B. V.; Kim, D. I.; Shivega, W. G.; Ali, M. H.; Faustino, R. S.; Campos, A. R.; Roux, K. J. VRK2A Is an A-Type Lamin–Dependent Nuclear Envelope Kinase That Phosphorylates BAF. *Mol. Biol. Cell* **2017**, *28* (17), 2241–2250. https://doi.org/10.1091/mbc.e17-03-0138.
(28) Aihara, H.; Nakagawa, T.; Mizusaki, H.; Yoneda, M.; Kato, M.; Doiguchi, M.; Imamura, Y.; Higashi, M.; Ikura, T.; Hayashi, T.; Kodama, Y.; Oki, M.; Nakayama, T.; Cheung, E.; Aburatani, H.; Takayama, K.; Koseki, H.; Inoue, S.; Takeshima, Y.; Ito, T. Histone H2A T120 Phosphorylation Promotes Oncogenic

Transformation via Upregulation of Cyclin D1. *Mol. Cell* **2016**, *64* (1), 176–188. https://doi.org/10.1016/j.molcel.2016.09.012.

(29) Kang, T.-H.; Park, D.-Y.; Choi, Y. H.; Kim, K.-J.; Yoon, H. S.; Kim, K.-T. Mitotic Histone H3 Phosphorylation by Vaccinia-Related Kinase 1 in Mammalian Cells. *Mol. Cell. Biol.* **2007**, *27* (24), 8533–8546. https://doi.org/10.1128/MCB.00018-07.

(30) Martín-Doncel, E.; Rojas, A. M.; Cantarero, L.; Lazo, P. A. VRK1 Functional Insufficiency Due to Alterations in Protein Stability or Kinase Activity of Human VRK1 Pathogenic Variants Implicated in Neuromotor Syndromes. *Sci. Rep.* **2019**, *9* (1), 13381. https://doi.org/10.1038/s41598-019-49821-7.

(31) Valbuena, A.; Sanz-García, M.; López-Sánchez, I.; Vega, F. M.; Lazo, P. A. Roles of VRK1 as a New Player in the Control of Biological Processes Required for Cell Division. *Cell. Signal.* **2011**, *23* (8), 1267–1272. https://doi.org/10.1016/j.cellsig.2011.04.002.

(32) Baker, S. J.; Fearon, E. R.; Nigro, J. M.; Hamilton, S. R.; Preisinger, A. C.; Jessup, J. M.; vanTuinen, P.; Ledbetter, D. H.; Barker, D. F.; Nakamura, Y.; White, R.; Vogelstein, B. Chromosome 17 Deletions and P53 Gene Mutations in Colorectal Carcinomas. *Science* **1989**, *244* (4901), 217–221. https://doi.org/10.1126/science.2649981.

(33) Hollstein, M.; Sidransky, D.; Vogelstein, B.; Harris, C. C. P53 Mutations in Human Cancers. *Science* **1991**, *253* (5015), 49–53. https://doi.org/10.1126/science.1905840.

(34) Kandoth, C.; McLellan, M. D.; Vandin, F.; Ye, K.; Niu, B.; Lu, C.; Xie, M.; Zhang, Q.; McMichael, J. F.; Wyczalkowski, M. A.; Leiserson, M. D. M.; Miller, C. A.; Welch, J. S.; Walter, M. J.; Wendl, M. C.; Ley, T. J.; Wilson, R. K.; Raphael, B. J.; Ding, L. Mutational Landscape and Significance across 12 Major Cancer Types. *Nature* **2013**, *502* (7471), 333–339. https://doi.org/10.1038/nature12634.

(35) Lawrence, M. S.; Stojanov, P.; Mermel, C. H.; Robinson, J. T.; Garraway, L. A.; Golub, T. R.; Meyerson, M.; Gabriel, S. B.; Lander, E. S.; Getz, G. Discovery and Saturation Analysis of Cancer Genes across 21 Tumour Types. *Nature* **2014**, *505* (7484), 495–501. https://doi.org/10.1038/nature12912.

(36) Hafner, A.; Bulyk, M. L.; Jambhekar, A.; Lahav, G. The Multiple Mechanisms That Regulate P53 Activity and Cell Fate. *Nat. Rev. Mol. Cell Biol.* **2019**, *20* (4), 199–210. https://doi.org/10.1038/s41580-019-0110-x.

(37) Serafim, R. A. M.; De Souza Gama, F. H.; Dutra, L. A.; Dos Reis, C. V.; Vasconcelos, S. N. S.; Da Silva Santiago, A.; Takarada, J. E.; Di Pillo, F.; Azevedo, H.; Mascarello, A.; Elkins, J. M.; Massirer, K. B.; Gileadi, O.; Guimarães, C. R. W.; Couñago, R. M. Development of Pyridine-Based Inhibitors for the Human Vaccinia-Related Kinases 1 and 2. *ACS Med. Chem. Lett.* **2019**, *10* (9), 1266–1271. https://doi.org/10.1021/acsmedchemlett.9b00082.

(38) Couñago, R. M.; Allerston, C. K.; Savitsky, P.; Azevedo, H.; Godoi, P. H.; Wells, C. I.; Mascarello, A.; De Souza Gama, F. H.; Massirer, K. B.; Zuercher, W. J.; Guimarães, C. R. W.; Gileadi, O. Structural Characterization of Human Vaccinia-Related Kinases (VRK) Bound to Small-Molecule Inhibitors Identifies Different P-Loop Conformations. *Sci. Rep.* **2017**, *7* (1), 7501. https://doi.org/10.1038/s41598-017-07755-y.

(39) Bain, J.; Plater, L.; Elliott, M.; Shpiro, N.; Hastie, C. J.; Mclauchlan, H.; Klevernic, I.; Arthur, J. S. C.; Alessi, D. R.; Cohen, P. The Selectivity of Protein Kinase Inhibitors: A Further Update. *Biochem. J.* **2007**, *408* (3), 297–315. https://doi.org/10.1042/BJ20070797.

(40) Sapkota, G. P.; Cummings, L.; Newell, F. S.; Armstrong, C.; Bain, J.; Frodin, M.; Grauert, M.; Hoffmann, M.; Schnapp, G.; Steegmaier, M.; Cohen, P.; Alessi, D. R. BI-D1870 Is a Specific Inhibitor of the P90 RSK (Ribosomal S6 Kinase) Isoforms *in Vitro* and *in Vivo*. *Biochem. J.* **2007**, *401* (1), 29–38. https://doi.org/10.1042/BJ20061088.

(41) Ciceri, P.; Müller, S.; O'Mahony, A.; Fedorov, O.; Filippakopoulos, P.; Hunt, J. P.; Lasater, E. A.; Pallares, G.; Picaud, S.; Wells, C.; Martin, S.; Wodicka, L. M.; Shah, N. P.; Treiber, D. K.; Knapp, S. Dual Kinase-Bromodomain Inhibitors for Rationally Designed Polypharmacology. *Nat. Chem. Biol.* **2014**, *10* (4), 305–312. https://doi.org/10.1038/nchembio.1471.

(42) Becher, I.; Savitski, M. M.; Savitski, M. F.; Hopf, C.; Bantscheff, M.; Drewes, G. Affinity Profiling of the Cellular Kinome for the Nucleotide Cofactors ATP, ADP, and GTP. *ACS Chem. Biol.* **2013**, *8* (3), 599–607. https://doi.org/10.1021/cb3005879.

(43) Zhang, L.; Holmes, I. P.; Hochgräfe, F.; Walker, S. R.; Ali, N. A.; Humphrey, E. S.; Wu, J.; De Silva, M.; Kersten, W. J. A.; Connor, T.; Falk, H.; Allan, L.; Street, I. P.; Bentley, J. D.; Pilling, P. A.; Monahan, B. J.; Peat, T. S.; Daly, R. J. Characterization of the Novel Broad-Spectrum Kinase Inhibitor CTx-0294885 As an Affinity Reagent for Mass Spectrometry-Based Kinome Profiling. *J. Proteome Res.* **2013**, *12* (7), 3104–3116. https://doi.org/10.1021/pr3008495.

(44) Couñago, R. M.; Allerston, C. K.; Savitsky, P.; Azevedo, H.; Godoi, P. H.; Wells, C. I.; Mascarello, A.; De Souza Gama, F. H.; Massirer, K. B.; Zuercher, W. J.; Guimarães, C. R. W.; Gileadi, O. Structural Characterization of Human Vaccinia-Related Kinases (VRK) Bound to Small-Molecule Inhibitors Identifies Different P-Loop Conformations. *Sci. Rep.* **2017**, *7* (1), 7501. https://doi.org/10.1038/s41598-017-07755-y.

(45) Jain, R.; Mathur, M.; Lan, J.; Costales, A.; Atallah, G.; Ramurthy, S.; Subramanian, S.; Setti, L.; Feucht, P.; Warne, B.; Doyle, L.; Basham, S.; Jefferson, A. B.; Lindvall, M.; Appleton, B. A.; Shafer, C. M. Discovery of Potent and Selective RSK Inhibitors as Biological Probes. *J. Med. Chem.* **2015**, *58* (17), 6766–6783. https://doi.org/10.1021/acs.jmedchem.5b00450.

(46) Baker, N. A.; Sept, D.; Joseph, S.; Holst, M. J.; McCammon, J. A. Electrostatics of Nanosystems: Application to Microtubules and the Ribosome. *Proc. Natl. Acad. Sci.* **2001**, *98* (18), 10037–10041. https://doi.org/10.1073/pnas.181342398.

(47) Filippakopoulos, P.; Picaud, S.; Mangos, M.; Keates, T.; Lambert, J.-P.; Barsyte-Lovejoy, D.; Felletar, I.; Volkmer, R.; Müller, S.; Pawson, T.; Gingras, A.-C.; Arrowsmith, C. H.; Knapp, S. Histone Recognition and Large-Scale Structural Analysis of the Human Bromodomain Family. *Cell* **2012**, *149* (1), 214–231. https://doi.org/10.1016/j.cell.2012.02.013.

(48) Elkins, J. M.; Fedele, V.; Szklarz, M.; Abdul Azeez, K. R.; Salah, E.; Mikolajczyk, J.; Romanov, S.; Sepetov, N.; Huang, X.-P.; Roth, B. L.; Al Haj Zen, A.; Fourches, D.; Muratov, E.; Tropsha, A.; Morris, J.; Teicher, B. A.; Kunkel, M.; Polley, E.; Lackey, K. E.; Atkinson, F. L.; Overington, J. P.; Bamborough, P.; Müller, S.; Price, D. J.; Willson, T. M.; Drewry, D. H.; Knapp, S.; Zuercher, W. J. Comprehensive Characterization of the Published Kinase Inhibitor Set. *Nat. Biotechnol.* **2016**, *34* (1), 95–103. https://doi.org/10.1038/nbt.3374.

(49) Rihtar, E.; Lebar, T.; Lainšček, D.; Kores, K.; Lešnik, S.; Bren, U.; Jerala, R. Chemically Inducible Split Protein Regulators for Mammalian Cells. *Nat. Chem. Biol.* **2023**, *19* (1), 64–71. https://doi.org/10.1038/s41589-022-01136-x.

(50) Brian Houston, J. Utility of in Vitro Drug Metabolism Data in Predicting in Vivo Metabolic Clearance. *Biochem. Pharmacol.* **1994**, *47* (9), 1469–1479. https://doi.org/10.1016/0006-2952(94)90520-7.

(51) Wenlock, M. C.; Austin, R. P.; Barton, P.; Davis, A. M.; Leeson, P. D. A Comparison of Physiochemical Property Profiles of Development and Marketed Oral Drugs. *J. Med. Chem.* **2003**, *46* (7), 1250–1256. https://doi.org/10.1021/jm021053p.

(52) Colmenero-Repiso, A.; Gómez-Muñoz, M. A.; Rodríguez-Prieto, I.; Amador-Álvarez, A.; Henrich, K.-O.; Pascual-Vaca, D.; Okonechnikov, K.; Rivas, E.; Westermann, F.; Pardal, R.; Vega, F. M. Identification of VRK1 as a New Neuroblastoma Tumor Progression Marker Regulating Cell Proliferation. *Cancers* **2020**, *12* (11), 3465. https://doi.org/10.3390/cancers12113465.

(53) Campillo-Marcos, I.; García-González, R.; Navarro-Carrasco, E.; Lazo, P. A. The Human VRK1 Chromatin Kinase in Cancer Biology. *Cancer Lett.* **2021**, *503*, 117–128. https://doi.org/10.1016/j.canlet.2020.12.032.

(54) Lee, N.; Kwon, J.-H.; Kim, Y. B.; Kim, S.-H.; Park, S. J.; Xu, W.; Jung, H.-Y.; Kim, K.-T.; Wang, H. J.; Choi, K. Y. Vaccinia-Related Kinase 1 Promotes Hepatocellular Carcinoma by Controlling the Levels of Cell

Cycle Regulators Associated with G1/S Transition. *Oncotarget* **2015**, *6* (30), 30130–30148. https://doi.org/10.18632/oncotarget.4967.

(55) Rampersad, S. N. Multiple Applications of Alamar Blue as an Indicator of Metabolic Function and Cellular Health in Cell Viability Bioassays. *Sensors* **2012**, *12* (9), 12347–12360. https://doi.org/10.3390/s120912347.

(56) Salzano, M.; Sanz-García, M.; Monsalve, D. M.; Moura, D. S.; Lazo, P. A. VRK1 Chromatin Kinase Phosphorylates H2AX and Is Required for Foci Formation Induced by DNA Damage. *Epigenetics* **2015**, *10* (5), 373–383. https://doi.org/10.1080/15592294.2015.1028708.

(57) Samwer, M.; Schneider, M. W. G.; Hoefler, R.; Schmalhorst, P. S.; Jude, J. G.; Zuber, J.; Gerlich, D. W. DNA Cross-Bridging Shapes a Single Nucleus from a Set of Mitotic Chromosomes. *Cell* **2017**, *170* (5), 956-972.e23. https://doi.org/10.1016/j.cell.2017.07.038.

(58) Molitor, T. P.; Traktman, P. Depletion of the Protein Kinase VRK1 Disrupts Nuclear Envelope Morphology and Leads to BAF Retention on Mitotic Chromosomes. *Mol. Biol. Cell* **2014**, *25* (6), 891–903. https://doi.org/10.1091/mbc.e13-10-0603.

(59) Cullen, C. F.; Brittle, A. L.; Ito, T.; Ohkura, H. The Conserved Kinase NHK-1 Is Essential for Mitotic Progression and Unifying Acentrosomal Meiotic Spindles in *Drosophila Melanogaster*. *J. Cell Biol.* **2005**, *171* (4), 593–602. https://doi.org/10.1083/jcb.200508127.

(60) Monsalve, D. M.; Campillo-Marcos, I.; Salzano, M.; Sanz-García, M.; Cantarero, L.; Lazo, P. A. VRK1 Phosphorylates and Protects NBS1 from Ubiquitination and Proteasomal Degradation in Response to DNA Damage. *Biochim. Biophys. Acta BBA - Mol. Cell Res.* **2016**, *1863* (4), 760–769. https://doi.org/10.1016/j.bbamcr.2016.02.005.

(61) Salzano, M.; Vázquez-Cedeira, M.; Sanz-García, M.; Valbuena, A.; Blanco, S.; Fernández, I. F.; Lazo, P. A. Vaccinia-Related Kinase 1 (VRK1) Confers Resistance to DNA-Damaging Agents in Human Breast Cancer by Affecting DNA Damage Response. *Oncotarget* **2014**, *5* (7), 1770–1778. https://doi.org/10.18632/oncotarget.1678.

(62) Gallego-Jara, J.; Lozano-Terol, G.; Sola-Martínez, R. A.; Cánovas-Díaz, M.; De Diego Puente, T. A Compressive Review about Taxol®: History and Future Challenges. *Molecules* **2020**, *25* (24), 5986. https://doi.org/10.3390/molecules25245986.

(63) Manfredi, M. G.; Ecsedy, J. A.; Chakravarty, A.; Silverman, L.; Zhang, M.; Hoar, K. M.; Stroud, S. G.; Chen, W.; Shinde, V.; Huck, J. J.; Wysong, D. R.; Janowick, D. A.; Hyer, M. L.; LeRoy, P. J.; Gershman, R. E.; Silva, M. D.; Germanos, M. S.; Bolen, J. B.; Claiborne, C. F.; Sells, T. B. Characterization of Alisertib (MLN8237), an Investigational Small-Molecule Inhibitor of Aurora A Kinase Using Novel *In Vivo* Pharmacodynamic Assays. *Clin. Cancer Res.* **2011**, *17* (24), 7614–7624. https://doi.org/10.1158/1078-0432.CCR-11-1536.

(64) Roth, A.; Gihring, A.; Bischof, J.; Pan, L.; Oswald, F.; Knippschild, U. CK1 Is a Druggable Regulator of Microtubule Dynamics and Microtubule-Associated Processes. *Cancers* **2022**, *14* (5), 1345. https://doi.org/10.3390/cancers14051345.

(65) Shrestha, A.; Hamilton, G.; O'Neill, E.; Knapp, S.; Elkins, J. M. Analysis of Conditions Affecting Auto-Phosphorylation of Human Kinases during Expression in Bacteria. *Protein Expr. Purif.* **2012**, *81* (1), 136–143. https://doi.org/10.1016/j.pep.2011.09.012.

(66) Newman, J. Novel Buffer Systems for Macromolecular Crystallization. *Acta Crystallogr. D Biol. Crystallogr.* **2004**, *60* (3), 610–612. https://doi.org/10.1107/S0907444903029640.

(67) Kabsch, W. *XDS*. *Acta Crystallogr. D Biol. Crystallogr.* **2010**, *66* (2), 125–132. https://doi.org/10.1107/S0907444909047337.

(68) Winn, M. D.; Ballard, C. C.; Cowtan, K. D.; Dodson, E. J.; Emsley, P.; Evans, P. R.; Keegan, R. M.; Krissinel, E. B.; Leslie, A. G. W.; McCoy, A.; McNicholas, S. J.; Murshudov, G. N.; Pannu, N. S.; Potterton, E. A.; Powell, H. R.; Read, R. J.; Vagin, A.; Wilson, K. S. Overview of the *CCP* 4 Suite and

Current Developments. *Acta Crystallogr. D Biol. Crystallogr.* **2011**, *67* (4), 235–242. https://doi.org/10.1107/S0907444910045749.

(69) McCoy, A. J.; Grosse-Kunstleve, R. W.; Adams, P. D.; Winn, M. D.; Storoni, L. C.; Read, R. J. *Phaser* Crystallographic Software. *J. Appl. Crystallogr.* **2007**, *40* (4), 658–674. https://doi.org/10.1107/S0021889807021206.

(70) Murshudov, G. N.; Skubák, P.; Lebedev, A. A.; Pannu, N. S.; Steiner, R. A.; Nicholls, R. A.; Winn, M. D.; Long, F.; Vagin, A. A. *REFMAC* 5 for the Refinement of Macromolecular Crystal Structures. *Acta Crystallogr. D Biol. Crystallogr.* **2011**, *67* (4), 355–367. https://doi.org/10.1107/S0907444911001314.

(71) Emsley, P.; Lohkamp, B.; Scott, W. G.; Cowtan, K. Features and Development of *Coot*. *Acta Crystallogr. D Biol. Crystallogr.* **2010**, *66* (4), 486–501. https://doi.org/10.1107/S0907444910007493.

(72) Chen, V. B.; Arendall, W. B.; Headd, J. J.; Keedy, D. A.; Immormino, R. M.; Kapral, G. J.; Murray, L. W.; Richardson, J. S.; Richardson, D. C. *MolProbity* : All-Atom Structure Validation for Macromolecular Crystallography. *Acta Crystallogr. D Biol. Crystallogr.* **2010**, *66* (1), 12–21. https://doi.org/10.1107/S0907444909042073.

(73) Wu, Q.; Heidenreich, D.; Zhou, S.; Ackloo, S.; Krämer, A.; Nakka, K.; Lima-Fernandes, E.; Deblois, G.; Duan, S.; Vellanki, R. N.; Li, F.; Vedadi, M.; Dilworth, J.; Lupien, M.; Brennan, P. E.; Arrowsmith, C. H.; Müller, S.; Fedorov, O.; Filippakopoulos, P.; Knapp, S. A Chemical Toolbox for the Study of Bromodomains and Epigenetic Signaling. *Nat. Commun.* **2019**, *10* (1), 1915. https://doi.org/10.1038/s41467-019-09672-2.

(74) Bauer, N.; Balourdas, D.-I.; Schneider, J. R.; Zhang, X.; Berger, L. M.; Berger, B.-T.; Klopp, N. A.; Siveke, J. T.; Knapp, S.; Joerger, A. C. *Development of Potent Dual BET/HDAC Inhibitors* via *Pharmacophore Merging and Structure-Guided Optimization*; preprint; Biochemistry, 2023. https://doi.org/10.1101/2023.07.18.547334.

(75) Cascales, H. S.; Burdova, K.; Middleton, A.; Kuzin, V.; Müllers, E.; Stoy, H.; Baranello, L.; Macurek, L.; Lindqvist, A. *Cyclin A2 Localises in the Cytoplasm at the S/G2 Transition to Activate PLK1*; preprint; Cell Biology, 2017. https://doi.org/10.1101/191437.